energies

Article

Techno-Economic Optimization and Intelligent Energy Management of Grid-Connected PV-Wind Hydrogen Refueling Stations Under Long-Term Renewable Variability

Mahmoud El Amri [1], Ferdaws Ben Naceur [2], Mohamed Ali Zdiri [3,4,*], Ahmed Ali [5,*] and Chokri Ben Salah [1,6]

[1] Laboratory of Automation, Electrical Systems and Environment (LASEE), University of Monastir, Monastir 5035, Tunisia; mahmoudelamri@gmail.com (M.E.A.); chokribs@yahoo.fr (C.B.S.)
[2] Laboratory of Advanced Technology and Intelligent Systems (LATIS), University of Sousse, Sousse 4023, Tunisia; swadref87@hotmail.com
[3] Control & Energy Management Laboratory, Sfax Engineering School, University of Sfax, Sfax 3038, Tunisia
[4] Center for Research on Microgrids (CROM), Huanjiang Laboratory, Zhuji, Shaoxing 311800, China
[5] Department of Electrical and Electronic Engineering Technology, University of Johannesburg, Johannesburg 2006, South Africa
[6] Higher Institute of Applied Sciences and Technology of Sousse (ISSAT Sousse), University of Sousse, Sousse 4003, Tunisia
* Correspondence: zdirimohamedali@gmail.com (M.A.Z.); aali@uj.ac.za (A.A.)

Abstract

This paper examines how long-term solar-wind complementarity changes the least-cost design of grid-connected hydrogen refueling stations. A common techno-economic model combines PV, wind, batteries, grid exchange, PEM electrolysis, compression, high-pressure storage and fuel cell backup, using eleven years of hourly ERA5-Land data (2015–2025) for Bizerte, Sousse, Gabès and Ben Guerdane. Particle swarm optimization, reproducible within 0.4% over ten runs, sizes the components under a reserve-aware strategy enforcing a hydrogen loss-of-supply probability below 2% and a renewable fraction of at least 90%. The LCOH is 7.52, 7.88, 8.11 and 9.00 USD/kg at Bizerte, Gabès, Ben Guerdane and Sousse, with no unserved hydrogen demand. Bizerte, the least sunny site, is the cheapest because 666 kW of wind complements 760 kWp of PV, whereas Sousse, with the weakest wind, needs 2159 kWp of PV. Hydrogen storage of 1.5–2.8 days and electrolyzers rated 1.6–2.5 times the mean load provide the flexibility; fuel cells are never selected with grid access, and batteries matter only below 120–150 USD/kWh. The 90% renewable target raises the LCOH by 5.6–15.0%, the loss of export revenue by 7–11% and moderate electrolyzer degradation by 11–19%. The ranking holds under a 20% wind speed correction and in 96% of 1000 Monte Carlo samples, so multi-year solar-wind behavior, not irradiation alone, should guide coastal station siting.

Keywords: renewable hydrogen; hydrogen refueling station; PEM electrolysis; PV-wind hybrid system; techno-economic optimization; particle swarm optimization; energy management strategy; ERA5-Land

Academic Editor: Pavlos S. Georgilakis

Received: 16 September 2026
Revised: 20 October 2026
Accepted: 22 October 2026
Published: 20 November 2026

Copyright: © 2026 by the authors. Licensee MDPI, Basel, Switzerland. This article is an open access article distributed under the terms and conditions of the Creative Commons Attribution (CC BY) license.

1. Introduction

1.1. Background and Motivation

The decarbonization of energy and transport has increased interest in renewable hydrogen produced by renewable-powered water electrolysis. Hydrogen can support applications that are difficult to electrify directly, including heavy industry, long-haul transport, and seasonal energy storage [1,2]. Its economic viability remains strongly dependent on electricity cost, electrolyzer capital expenditure, utilization, and the temporal availability of renewable power [1,3,4]. PEM electrolysis is attractive for variable renewable generation because of its rapid response and broad operating range, although stack degradation, capital cost, and part-load operation remain important design considerations [3,5]. These effects are examined here through part-load and degradation sensitivity cases. Recent system-level studies further show that reliable hydrogen supply can require additional renewable and storage capacity when production is constrained by variable solar and wind resources [6].

North Africa, and Tunisia in particular, combines strong solar irradiation, useful coastal wind resources, and proximity to European energy markets, which has encouraged interest in renewable hydrogen development [7–9]. For refueling applications, on-site electrolysis can reduce dependence on hydrogen transport and can use locally available renewable electricity [10–13]. Electrolysis requires high-purity water, so water treatment or desalination becomes relevant as deployment scales in arid coastal regions [4,14]. The present study focuses on the energy system and does not model desalination explicitly. Its central questions are whether long-term solar-wind complementarity changes the preferred component mix across sites, and how the station should be sized and dispatched to supply hydrogen reliably at minimum cost.

1.2. Related Work

On-site hydrogen refueling stations. Recent HRS studies cover a wide range of scales and operating structures. Zúñiga-Saiz and Sánchez-Díaz [10] sized an electrolysis-based station for a bus fleet, while Mahmood et al. [11] evaluated a PV-powered station for railway demand. Cardona et al. developed detailed station models and control strategies [15,16], and Kim et al. [17] incorporated electrolyzer degradation and multistage compression into profit-oriented operation. Grid-connected bus-fleet HRS sizing has also been examined by Caponi et al. [12], while Hajjaji and Cristofari [13] analyzed a 440 kg/day solar HRS in Corsica. Wu et al. [18] further showed that the electricity procurement of an on-site HRS depends on the market and tariff structure, which motivates the tariff scenarios examined here. These studies demonstrate the technical diversity of HRS design, but most focus on a single location or a prescribed generation and storage architecture.

Sizing and energy management of hybrid renewable systems. Hybrid renewable sizing has been studied for PV/wind/battery microgrids [19–22] and for hydrogen production systems [23–26]. Li et al. [25] optimized a wind-PV-electrolysis-battery system using a representative meteorological year, while Al-Mahmodi et al. [26] quantified the sensitivity of PV-wind hydrogen economics to electrolyzer and electricity-cost parameters. Oueslati and Fezai [27] compared PV-wind hydrogen refueling configurations across 20 Saudi sites, and Haffaf and Lakdja [28] examined solar-wind complementarity for large-scale hydrogen production in Algeria. These contributions confirm the importance of location and renewable mix, but they address different system boundaries, scales, data horizons, or technology-selection rules from those considered here.

Optimization methods. Metaheuristics are widely applied to non-convex and mixed-integer sizing problems. PSO remains a common benchmark because of its simple implementation and established use in hybrid-system design [19,29,30]. Other studies apply

improved swarm methods [29] or multi-objective formulations that trade cost against productivity [24,31]. The methodological contribution of the present work is therefore not the introduction of a new metaheuristic. Instead, PSO is used as a transparent search layer around a long-horizon, reserve-aware dispatch model so that renewable generation, battery capacity, hydrogen storage, fuel-cell backup, and grid interaction are evaluated on the same economic and reliability basis.

Component technologies and storage economics. PEM electrolyzers, fuel cells, and storage technologies have been extensively characterized at component and system levels [4,5,23,32]. Beuse et al. [33] showed that the preferred storage technology depends on cost, application, and time horizon rather than following a universal ranking. Recent reviews similarly identify compressed hydrogen as an economically relevant storage option in many renewable hydrogen configurations while stressing that optimal architecture remains application-specific [4]. This evidence supports treating battery capacity, compressed-hydrogen buffering, and fuel-cell backup as competing design options rather than mandatory components.

Solar-wind complementarity. Temporal complementarity between solar and wind generation can smooth renewable supply and reduce balancing requirements. This effect has been quantified for North Africa [34], sub-Saharan locations [35], Algeria [28], and broader open-data applications [36]. However, resource complementarity is often reported as a meteorological indicator or is embedded in a pre-defined system configuration. Fewer studies quantify whether wind capacity is retained by a cost-minimizing HRS design once grid exchange, electrolysis, hydrogen storage, battery storage, and reliability constraints are evaluated simultaneously over many years.

Table 1 positions the present study against recent work most closely related to renewable hydrogen production and refueling. The comparison is intended to clarify the system boundary and evidence base rather than to imply direct equivalence among studies with different scales, tariffs, and demand profiles.

Table 1. Comparison with recent studies.

Study	System	Spatial/Data Scope	Grid Context	Sizing/Operation Focus	Difference from Present Study
Cardona et al. [15,16]	On-site HRS with electrolysis, compression and storage	Single station case	Station-level operation	Finite-state and MPC operation	Control-oriented; no four-site multi-year sizing comparison
Roslan et al. [37]	Renewable H_2 storage with EV charging	Several Malaysian locations	Grid-connected	Techno-economic location comparison	Different end-use and architecture
Park et al. [24]	Solar-powered hydrogen plant	Single-resource cases	Plant-level	Multi-objective sizing	PV-focused; no solar-wind site complementarity
Caponi et al. [12]	Electrolysis HRS for bus fleets	Fleet scenarios	Grid-connected	Techno-economic sizing	No long-term multi-site renewable co-design
Oueslati and Fezai [27]	PV-wind HRS	20 Saudi sites	Autonomous configurations	HOMER-based scenario sizing	Storage/generation scenarios prescribed in advance
Haffaf and Lakdja [28]	Solar-wind H_2 production and storage	Multiple Algerian climates	Large-scale plant	Techno-economic complementarity assessment	Not a refueling-station dispatch problem
Li et al. [25]	Wind-PV-electrolysis-battery	Representative meteorological year	Power and H_2 plant	Capacity optimization	Uses representative-year rather than 11-year hourly evaluation
O'Neill et al. [6]	Solar/wind electrolysis with storage	Multiple Australian locations; hourly weather	Grid/backup scenarios	Reliable hydrogen-output design	Hydrogen-production focus rather than HRS technology selection

Hajjaji and Cristofari [13]	Solar HRS	Ajaccio; 440 kg/day	Single site	Techno-economic assessment	PV-only and single-site
Present study	PV-wind-battery-grid HRS with PEM electrolysis, H_2 storage and optional fuel cell	Four Tunisian coastal sites; 2015–2025 hourly data	Bidirectional grid	PSO sizing with reserve-aware hourly dispatch	Endogenous technology selection with multi-year reliability and solar-wind complementarity

1.3. Research Gaps

The comparative review above identifies five gaps that define the scope of this study:

- **G1. Multi-year resource representation.** Many published sizing studies rely on a typical meteorological year, a short measurement period, or a single representative year. Such approaches can miss inter-annual variability and extended low-resource sequences that influence hydrogen storage and reliability [6,25].
- **G2. Multi-site transferability.** Multi-location studies exist [27,28,37], but fewer combine several sites with the same hourly dispatch model and a decade-scale resource record, which is needed to isolate the effect of contrasting coastal solar-wind regimes on design.
- **G3. Technology selection within optimization.** Battery storage, compressed-hydrogen buffering, fuel-cell backup, and wind capacity are often prescribed through predefined configurations or scenarios [23,25,27]. Their relative economic value is therefore not always tested within one common design space.
- **G4. Integrated sizing and dispatch.** HRS control and plant sizing are frequently treated as separate problems [12,15,16]. A transparent formulation that links hourly reserve-aware operation to component sizing over a long meteorological record remains comparatively less explored for grid-connected renewable HRS.
- **G5. Interpretation of technology selection.** Techno-economic studies commonly report optimal capacities, but the physical reason for excluding a technology or for favoring one renewable source can receive limited attention. This interpretation is important when results are transferred to planning decisions.

1.4. Contributions of This Work

To address these gaps, this paper uses an established optimization method within a site-resolved framework designed to isolate the techno-economic value of long-term solar-wind complementarity. The component models, the rule-based dispatch, and PSO are established methods; the contribution lies in their combination over a decade-scale, multi-site record and in the systematic testing of the resulting technology selection. The main contributions are:

1. **Transparent station model.** A transparent station model covering PV, wind, battery storage, grid exchange, PEM electrolysis, compression, high-pressure hydrogen storage, optional PEM fuel-cell backup, and power conversion. The physical and economic relations are stated through numbered equations and literature-based parameters.
2. **Decade-scale multi-site assessment.** A common 11-year hourly assessment (2015–2025; 96,432 time steps per site) for Bizerte, Sousse, Gabès, and Ben Guerdane, allowing the same dispatch and reliability criteria to be applied to contrasting coastal resource regimes.
3. **Integrated sizing and dispatch.** A reserve-aware rule-based EMS is nested inside the PSO sizing loop, so every candidate design is evaluated over the full meteorological record against the same hydrogen-supply and renewable-fraction constraints.

4. **Endogenous technology selection.** Endogenous technology selection across PV, wind, battery storage, grid exchange, electrolysis, compression, hydrogen storage, and fuel-cell backup, avoiding a priori selection of the final storage and backup mix.
5. **Interpretation of design outcomes.** A quantitative interpretation of non-obvious design outcomes, particularly the exclusion of fuel-cell capacity under the base-case grid conditions, the scenario-dependent battery-cost threshold, and the site-dependent economic value of wind generation.
6. **Site-resolved comparison.** A site-resolved comparison of LCOH, renewable fraction, grid exchange, hydrogen reliability, and optimal capacities that directly links solar-wind complementarity to station design and cost.
7. **Robustness and uncertainty assessment.** Ten independent PSO runs per site, scenarios for wind data bias, export restrictions, tariffs, grid outages, demand profiles, and electrolyzer degradation, and a 1000-sample Monte Carlo analysis separate the robust conclusions from those that remain conditional on the assumptions.

1.5. Paper Organization

The remainder of the paper is organized as follows. Section 2 describes the system architecture, component models, reserve-aware energy management, sizing formulation, and the assumptions used for data and economic interpretation. Section 3 presents the resource, sizing, operational, sensitivity, robustness and uncertainty results. Section 4 compares the findings with recent literature, discusses practical implications and transferability, and states the main limitations. Section 5 summarizes the conclusions.

2. Materials and Methods

2.1. System Architecture and Energy Flows

The system is a grid-connected hybrid power plant supplying a renewable hydrogen refueling station (HRS). A common DC bus links the photovoltaic (PV) array, wind turbine, lithium-iron-phosphate battery, bidirectional grid interface, PEM electrolyzer, multistage hydrogen compressor, high-pressure storage tank, and PEM fuel cell. DC/DC and DC/AC converters provide the required power conditioning. The battery supports short-term balancing, the electrolyzer produces hydrogen on site, the compressor feeds the storage tank, and the fuel cell is available as dispatchable backup. The configuration is consistent with previously reported grid-connected hybrid hydrogen systems [15,20,23] and is shown in Figure 1.

Model parameters are referenced to the MINCATEC Autonomous Multifunction Hydrogen Station (manufacturer technical proposal), whose component specifications are summarized in Table 2. Two modifications are introduced to represent station-scale operation. First, the demonstrator uses low-pressure metal-hydride tanks (1 kg H_2 per 85 kg tank; absorption/desorption energy < 4 kWh/kg), whereas the present model uses compressed-gas storage because it is more suitable for the throughput considered here. Second, the demonstrator is autonomous and uses fuzzy-logic control, whereas the system analyzed in this study is grid connected and dispatched by the reserve-aware rule-based strategy described in Section 2.11. Component capacities are optimized rather than fixed to the demonstrator ratings. Although coastal water treatment is relevant to renewable hydrogen production, a dedicated SWRO unit is not included in the present sizing or EMS. At the 100 kg H_2/day case-study demand, the stoichiometric water requirement is approximately 0.9 m^3/day (9 kg H_2O/kg H_2; Section 2.5). Using a representative SWRO electricity requirement of 3.5 kWh/m^3 [14], desalination would consume about 3.2 kWh/day, compared with 5.0–5.5 MWh/day for electrolysis at 50–55 kWh/kg H_2. Its electrical contribution is therefore approximately 0.06%, and remains well below 0.15% of the

electrolyzer load at the planning scale considered here. Desalination is consequently excluded from the present EMS and techno-economic sizing so that the analysis remains focused on the dominant station energy flows.

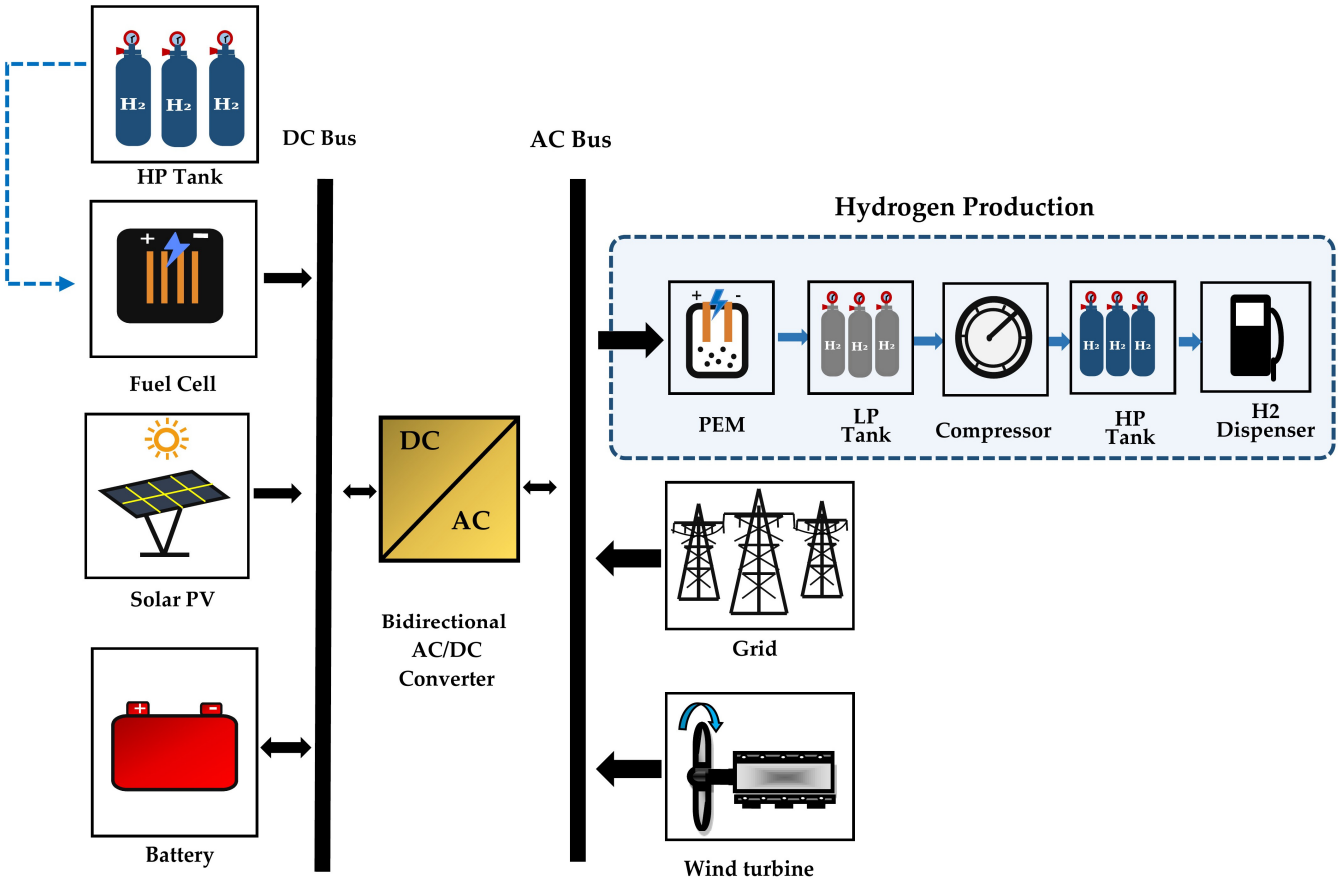

Figure 1. Grid-connected PV-wind-battery HRS.

Table 2. MINCATEC specifications used for parameterization.

Component	Demonstrator Specification	Use in Model
PV array	30 modules, 1.83 m² each, ≈55 m², 10 kW, tilt 36°	module area, tilt, derating
Wind	(not included in demonstrator)	Literature-based turbine curve
Battery	Pylontech LFP, 48 V, 28 kWh, 6000 cycles at 80% DoD	η_{ch}, η_{dis}, DoD, cycle life
Electrolyzer	PEM, 5.5 kW, 50 bar outlet, >99.995% purity, 5 L/h demineralized water, 1.3 kW heat	rated power, outlet pressure, water rate
Fuel cell	Proton Motor S8, 8.4 kW, system efficiency 57%, 0.55 kg/h	$\eta_{fc} = 0.57$
H_2 storage	Metal-hydride storage, 1 kg/tank (model uses compressed gas)	Scaled to compressed-gas storage
Cost reference	electrolyzer 82 988 €, 10 kW PV 27 840 €, fuel-cell system 69 600 €, H_2 storage 33 600 €, total ≈ 344 941 €	Demonstrator-scale cost reference

All state variables are propagated on the native hourly ERA5-Land time step ($\Delta t = 1$ h) over the 2015–2025 record.

2.2. Photovoltaic Model

The module cell temperature is obtained from the nominal-operating-cell-temperature (NOCT) model [20,23]:

$$T_{cell}(t) = T_{amb}(t) + \frac{NOCT - 20}{800} G(t) \quad (1)$$

where G is the plane-of-array irradiance (W/m²) and T_{amb} is the ambient temperature (°C). The array output power is [20,23]:

$$P_{\mathrm{PV}}(t) = N_{\mathrm{PV}}\, P_{\mathrm{STC}}\, \frac{G(t)}{G_{\mathrm{STC}}} [1 + \gamma_P (T_{\mathrm{cell}}(t) - T_{\mathrm{STC}})]\, \eta_{\mathrm{dr}} \tag{2}$$

where P_{STC} is the module rating at standard test conditions ($G_{\mathrm{STC}} = 1000$ W/m², $T_{\mathrm{STC}} = 25$ °C), $\gamma_P < 0$ is the power-temperature coefficient, and η_{dr} is the soiling and wiring de-rating factor. The occupied area is calculated from the module count:

$$A_{\mathrm{PV}} = N_{\mathrm{PV}}\, A_{\mathrm{mod}} \tag{3}$$

In the base case, G is set equal to the ERA5-Land global horizontal irradiance, so the transposition gain of the 36° demonstrator tilt is neglected. This choice is conservative: a transposition test with the Erbs decomposition and an isotropic sky model raised the specific PV yield by 6–8% and lowered the LCOH of the PV-dominated Sousse design by about 4%. The base-case values $\mathrm{NOCT} = 45$ °C, $\gamma_P = -0.4$ %/K and $\eta_{\mathrm{dr}} = 0.86$ give specific yields of 1402–1560 kWh/kWp per year at the four sites.

2.3. Wind-Turbine Model

Air density is corrected for site pressure and temperature from the ideal-gas law [19,20]:

$$\rho_a(t) = \frac{p_{\mathrm{sp}}(t)}{R_a\, T^{\mathrm{K}}_{\mathrm{amb}}(t)} \tag{4}$$

where $R_a = 287.05$ J/kg/K is the specific gas constant for dry air. The 10 m ERA5-Land wind speed is extrapolated to hub height z_h by the power law [34,35]:

$$v_h(t) = v_{10}(t) \left(\frac{z_h}{z_{10}}\right)^{\alpha} \tag{5}$$

where $\alpha = 1/7$ is the shear exponent and $z_h = 80$ m is the hub height. The mechanical output uses the standard piecewise power curve [20,29]:

$$P_{\mathrm{WT}}(v_h) = \begin{cases} 0, & v_h < v_{ci} \text{ or } v_h \geq v_{co} \\ P_r\, \dfrac{v_h^3 - v_{ci}^3}{v_r^3 - v_{ci}^3}, & v_{ci} \leq v_h < v_r \\ P_r, & v_r \leq v_h < v_{co} \end{cases} \tag{6}$$

where v_{ci} is the cut-in speed, v_r is the rated speed, and v_{co} is the cut-out speed ($v_{ci} = 3$ m/s, $v_r = 11.5$ m/s and $v_{co} = 25$ m/s for the generic turbine curve). Output is corrected for instantaneous air density [19]:

$$P^{\rho}_{\mathrm{WT}}(t) = P_{\mathrm{WT}}\big(v_h(t)\big)\, \frac{\rho_a(t)}{\rho_0} \tag{7}$$

where $\rho_0 = 1.225$ kg/m³ is the reference air density.

For resource characterization the wind distribution is fitted to a two-parameter Weibull law [34,35]:

$$f(v) = \frac{k}{c} \left(\frac{v}{c}\right)^{k-1} \exp\left[-\left(\frac{v}{c}\right)^{k}\right] \tag{8}$$

where k is the Weibull shape parameter and c (m/s) is the scale parameter, both fitted by maximum likelihood to the hub-height series.

2.4. Battery Model

The battery energy content evolves with charge and discharge efficiencies η_{ch} and η_{dis} [19,20]:

$$E_b(t+1) = E_b(t) + \left(\eta_{\mathrm{ch}}\, P_b^{\mathrm{ch}}(t) - \frac{P_b^{\mathrm{dis}}(t)}{\eta_{\mathrm{dis}}}\right)\Delta t \tag{9}$$

The state of charge is defined as:

$$\mathrm{SOC}(t) = \frac{E_b(t)}{E_b^{\mathrm{cap}}} \tag{10}$$

The battery is subject to depth-of-discharge and power limits [20]:

$$\mathrm{SOC}_{\min} \le \mathrm{SOC}(t) \le \mathrm{SOC}_{\max}, \qquad 0 \le P_b^{\mathrm{ch,dis}}(t) \le P_b^{\max} \tag{11}$$

with $\mathrm{SOC}_{\min} = 0.2$, $\mathrm{SOC}_{\max} = 1$, $P_b^{\max} = 0.5\, E_b^{\mathrm{cap}}$ and $\eta_{\mathrm{ch}} = \eta_{\mathrm{dis}} = 0.95$.

Calendar and cycle ageing are represented through an equivalent-throughput lifetime [33]:

$$L_b = \min\left(L_b^{\mathrm{cal}}, \frac{N_{\mathrm{cyc}}\, \mathrm{DoD}\, E_b^{\mathrm{cap}}}{\sum_{t\in \mathrm{yr}} P_b^{\mathrm{dis}}(t)\, \Delta t}\right) \tag{12}$$

where N_{cyc} is the rated cycle life at the reference DoD (6000 cycles at 80% for the LFP pack of Table 2) and $L_b^{\mathrm{cal}} = 15$ years is the calendar limit. Only the discharge throughput enters the denominator, so that each equivalent full cycle is counted once.

2.5. PEM Electrolyzer Model

Hydrogen mass production is proportional to the electrical input through the electrolyzer efficiency [5,20]:

$$\dot{m}_{\mathrm{H_2}}^{\mathrm{el}}(t) = \frac{\eta_{\mathrm{el}}\, P_{\mathrm{el}}(t)}{\mathrm{HHV}_{\mathrm{H_2}}} \tag{13}$$

where $\mathrm{HHV}_{\mathrm{H_2}} = 39.4$ kWh/kg is the hydrogen higher heating value. At stack level, the molar production rate follows Faraday's law [5]:

$$\dot{n}_{\mathrm{H_2}}(t) = \eta_F\, \frac{N_c\, I_{\mathrm{el}}(t)}{2F} \tag{14}$$

where N_c is the number of series cells, η_F is the Faraday efficiency, and F is Faraday's constant. The system-specific energy consumption is defined as:

$$\mathrm{SEC}(t) = \frac{P_{\mathrm{el}}(t)}{\dot{m}_{\mathrm{H_2}}^{\mathrm{el}}(t)} \tag{15}$$

A representative PEM specific energy consumption of 50–55 kWh/kg is reported for PEM systems [3,5]; the base case uses the upper value, $\mathrm{SEC} = 55$ kWh/kg at system level ($\eta_{\mathrm{el}} = 0.716$ on a higher heating value basis), consistent with the demonstrator rating in Table 2. Electrolyzer operation is limited by the stack turndown ratio [16]:

$$P_{\mathrm{el}}^{\min} \le P_{\mathrm{el}}(t) \le P_{\mathrm{el}}^{\mathrm{rated}} \tag{16}$$

with $P_{\mathrm{el}}^{\min} = 0.1\, P_{\mathrm{el}}^{\mathrm{rated}}$.

The ultrapure feedwater demand (stoichiometric plus purge/cooling surplus λ_w) is [5]:

$$\dot{m}_{\mathrm{H_2O}}(t) = (1+\lambda_w)\, \frac{M_{\mathrm{H_2O}}}{M_{\mathrm{H_2}}}\, \dot{m}_{\mathrm{H_2}}^{\mathrm{el}}(t) \tag{17}$$

This gives a stoichiometric minimum of approximately 9 kg of water per kg H_2; the demonstrator uses approximately 5 L/h of demineralized water at <2 µS/cm.

Part-load efficiency and degradation. In the base case, SEC is constant and the stack is replaced every 80,000 operating hours at 40% of the electrolyzer CAPEX, which corresponds to a voltage degradation of about 2.4 µV/h until a 10% end-of-life voltage increase

[38,39]. Because the variable renewable input causes part-load operation and frequent starts, two extensions are tested in Section 3.8. The first represents the load dependence of the system SEC through the stack polarization and a fixed balance-of-plant share,

$$\mathrm{SEC}(\lambda) = \mathrm{SEC}_r \left[\left(1 - \beta_{\mathrm{bop}}\right) \frac{V_0 + (V_r - V_0)\lambda}{V_r} + \frac{\beta_{\mathrm{bop}}}{\lambda} \right] \tag{17a}$$

where $\lambda = P_{\mathrm{el}}/P_{\mathrm{el}}^{\mathrm{rated}}$ is the load ratio, proportional to the stack current density at constant cell count, $V_0 = 1.55$ V and $V_r = 1.90$ V are the cell voltages at zero and rated current density, and $\beta_{\mathrm{bop}} = 0.04$ is the fixed auxiliary share. The curve reproduces the rated value, reaches its minimum near 40–50% load, and rises steeply below 15% load. The second extension accumulates degradation with operating time and starts,

$$\delta(t) = \frac{r_V}{V_r}\left[h_{\mathrm{op}}(t) + \kappa_{\mathrm{ss}}\, N_{\mathrm{ss}}(t)\right], \qquad \mathrm{SEC}(t) = \mathrm{SEC}(\lambda)[1 + \delta(t)] \tag{17b}$$

where r_V is the cell voltage degradation rate, h_{op} and N_{ss} are the operating hours and starts since the last stack replacement, and κ_{ss} converts a start into equivalent operating hours. The stack is replaced when δ reaches 0.10, and the resulting interval enters Equation (32). The moderate case D1 uses $r_V = 4$ µV/h and $\kappa_{\mathrm{ss}} = 10$ h, and the stress case D2 uses $r_V = 8$ µV/h and $\kappa_{\mathrm{ss}} = 30$ h; the degradation rates lie within the range reported for PEM stacks [38,39], whereas the start penalties are scenario assumptions. The stack temperature is assumed to be regulated near its nominal value, and operation at the 50 bar outlet pressure of Table 2 is included in the rated SEC; its Nernst penalty of about 3% is partly offset by the lower downstream compression ratio.

2.6. Compression and High-Pressure Storage

Compression to storage pressure uses an n_s-stage intercooled polytropic model [16,17]:

$$w_c = \frac{n_s\,\gamma}{\gamma - 1}\,\frac{R\,T_{\mathrm{in}}}{M_{\mathrm{H_2}}\,\eta_{\mathrm{is}}}\left[\left(\frac{p_{\mathrm{out}}}{p_{\mathrm{in}}}\right)^{\frac{\gamma-1}{n_s\gamma}} - 1\right] \tag{18}$$

where $\gamma = 1.41$ is the heat capacity ratio of hydrogen, $\eta_{\mathrm{is}} = 0.55$ is the overall compressor efficiency (isentropic, mechanical and drive), $n_s = 3$, $p_{\mathrm{in}} = 50$ bar, $p_{\mathrm{out}} = 900$ bar for 70 MPa dispensing to passenger cars, and $T_{\mathrm{in}} = 303$ K is the suction temperature restored by intercooling before each stage, which gives $w_c = 2.11$ kWh/kg. Because intercooling removes the heat of compression after each stage, the work scales linearly with the suction temperature; a sensitivity case therefore links it to the ambient temperature,

$$T_{\mathrm{in}}(t) = T_{\mathrm{amb}}(t) + \Delta T_{\mathrm{ic}} \tag{18a}$$

with an intercooler approach of $\Delta T_{\mathrm{ic}} = 10$ K (Section 3.8). The compressor electrical power is:

$$P_c(t) = \dot{m}^{c}_{\mathrm{H_2}}(t)\, w_c \tag{19}$$

The stored hydrogen mass follows the balance between production, dispensing, and fuel cell consumption [15]:

$$m_{\mathrm{st}}(t+1) = m_{\mathrm{st}}(t) + \left(\dot{m}^{c}_{\mathrm{H_2}}(t) - \dot{m}^{\mathrm{disp}}_{\mathrm{H_2}}(t) - \dot{m}^{\mathrm{fc}}_{\mathrm{H_2}}(t)\right)\Delta t \tag{20}$$

The tank pressure is calculated from the real-gas relation [16]:

$$p_{\mathrm{st}}(t) = \frac{Z\, m_{\mathrm{st}}(t)\, R\, T_{\mathrm{st}}}{M_{\mathrm{H_2}}\, V_{\mathrm{st}}} \tag{21}$$

where Z is the compressibility factor. The storage bounds are:

$$m_{\mathrm{st}}^{\min} \le m_{\mathrm{st}}(t) \le m_{\mathrm{st}}^{\max} \tag{22}$$

with $m_{\mathrm{st}}^{\min} = 0.1\, m_{\mathrm{st}}^{\max}$, the residual inventory needed to maintain the cascade pressure.

2.7. PEM Fuel-Cell Model

The fuel cell converts stored hydrogen back to electricity for backup [23,32]:

$$P_{\mathrm{fc}}(t) = \eta_{\mathrm{fc}}\, \dot{m}_{\mathrm{H_2}}^{\mathrm{fc}}(t)\, \mathrm{LHV}_{\mathrm{H_2}} \tag{23}$$

where $\mathrm{LHV}_{\mathrm{H_2}} = 33.3$ kWh/kg is the hydrogen lower heating value. Part-load efficiency is represented by [32]:

$$\eta_{\mathrm{fc}}(P_{\mathrm{fc}}) = \eta_{\mathrm{fc}}^{0}\left[a_0 + a_1 \frac{P_{\mathrm{fc}}}{P_{\mathrm{fc}}^{r}} + a_2 \left(\frac{P_{\mathrm{fc}}}{P_{\mathrm{fc}}^{r}}\right)^2\right] \tag{24}$$

The rated system efficiency is 57% (Table 2), the coefficients $a_0 = 1.10$, $a_1 = 0$ and $a_2 = -0.10$ give about 62% at 30% load, and the fuel cell power is constrained by:

$$P_{\mathrm{fc}}(t) \in \{0\} \cup \left[P_{\mathrm{fc}}^{\min},\, P_{\mathrm{fc}}^{r}\right], \qquad P_{\mathrm{fc}}^{\min} = 0.1\, P_{\mathrm{fc}}^{r} \tag{25}$$

The minimum load excludes the low-efficiency region in which auxiliary consumption dominates [32]. Requests below $P_{\mathrm{fc}}^{\min}$ are served by the grid; during grid outages, the fuel cell runs at its minimum load, and the surplus is curtailed. Fuel cell degradation enters the cost model through a stack replacement after 20,000 operating hours at 60% of the fuel cell CAPEX.

2.8. Power Conditioning and Grid Interface

Each power-conversion stage is represented by a constant-efficiency relation [21]:

$$P_{\mathrm{out}}(t) = \eta_{\mathrm{conv}}\, P_{\mathrm{in}}(t) \tag{26}$$

The instantaneous bus power balance is [19,21]:

$$P_{\mathrm{PV}} + P_{\mathrm{WT}}^{\rho} + P_{\mathrm{fc}} + P_{\mathrm{grid}}^{\mathrm{imp}} + P_{b}^{\mathrm{dis}} = P_{\mathrm{load}} + P_{\mathrm{el}} + P_{c} + P_{b}^{\mathrm{ch}} + P_{\mathrm{grid}}^{\mathrm{exp}} \tag{27}$$

The time index is omitted for clarity, and grid exchange is limited by the point-of-common-coupling rating:

$$0 \le P_{\mathrm{grid}}^{\mathrm{imp}}(t) \le P_{\mathrm{grid}}^{\max}, \qquad 0 \le P_{\mathrm{grid}}^{\mathrm{exp}}(t) \le P_{\mathrm{grid}}^{\max} \tag{28}$$

The PCC rating is 2 MW, which is not binding in the base case. Exports can also be capped at a fraction χ_{exp} of the annual on-site renewable production,

$$\sum_{t \in \mathrm{yr}} P_{\mathrm{grid}}^{\mathrm{exp}}(t)\, \Delta t \le \chi_{\mathrm{exp}} \sum_{t \in \mathrm{yr}} \left(P_{\mathrm{PV}}(t) + P_{\mathrm{WT}}^{\rho}(t)\right) \Delta t \tag{28a}$$

with $\chi_{\mathrm{exp}} = 1$ (no cap) in the base case and $\chi_{\mathrm{exp}} = 0.3$ in a regulatory case that reflects the 30% limit on surplus sales of the Tunisian self-generation regime [40]. The cap is enforced hourly on the running annual balance, without foresight.

2.9. Refueling Demand

The station follows a prescribed hydrogen dispensing profile $\dot{m}_{\mathrm{H_2}}^{\mathrm{disp}}(t)$ with annual demand:

$$M_{\mathrm{H_2}}^{\mathrm{yr}} = \sum_{t} \dot{m}_{\mathrm{H_2}}^{\mathrm{disp}}(t)\, \Delta t \tag{29}$$

The 100 kg H_2/day case-study demand, reported in Section 3, is interpreted as a station-scale light-duty mobility scenario representing the aggregate daily refueling requirement of a fleet of fuel-cell passenger cars, rather than a bus, rail, or bulk-industrial hydrogen duty. The same aggregate dispensing profile is applied at all four sites so that resource and sizing effects are compared on a common automotive-demand basis.

In the base case, the dispensing profile is uniform (4.17 kg/h), which isolates resource effects but ignores refueling peaks. Two alternative profiles are tested in Section 3.8: a diurnal profile with morning and late-afternoon peaks, of the type derived from gasoline-station data for HRS planning [41], whose peak hour carries 8.3% of the daily demand; and a stochastic profile that adds weekly factors of 1.05, 0.95 and 0.80 for weekdays, Saturdays and Sundays and a random daily variation with a coefficient of variation of 0.25, truncated to 0.4–1.6 times the mean, while preserving the annual total. The reserve of Equation (39) always uses the expected profile, so the stochastic case also tests the reserve rule against forecast errors. The station auxiliary load is $P_{\mathrm{load}}(t) = P_{\mathrm{aux}} + e_{\mathrm{disp}}\,\dot{m}_{\mathrm{H_2}}^{\mathrm{disp}}(t)$, with $P_{\mathrm{aux}} = 2$ kW and $e_{\mathrm{disp}} = 0.6$ kWh/kg for dispensing and pre-cooling.

2.10. Techno-Economic Model

Total installed capital cost is obtained by summing the component-specific unit costs c_i^{cap} multiplied by the corresponding ratings S_i [19,21]:

$$C_{\mathrm{cap}} = \sum_i c_i^{\mathrm{cap}}\, S_i \tag{30}$$

Capital costs are annualized using the capital recovery factor for discount rate d and project life N [19,22]:

$$\mathrm{CRF} = \frac{d\,(1+d)^N}{(1+d)^N - 1} \tag{31}$$

The present value of replacing components with lifetime $L_i < N$ shorter than the project life is calculated as [22,29]:

$$C_{\mathrm{rep},i} = \varphi_i\, c_i^{\mathrm{cap}}\, S_i \sum_{j=1}^{\lceil N/L_i \rceil - 1} \frac{1}{(1+d)^{jL_i}} \tag{32}$$

where φ_i is the replaced share of the component cost (0.4 for the electrolyzer stack, 0.6 for the fuel cell stack and 1 for the battery and the compressor, whose life is 15 years). The upper limit counts only replacements that occur before the end of the project life, and no salvage value is credited.

Annual operating cost includes fixed O&M and the net grid energy bill under import/export tariffs $\pi_{\mathrm{imp}}, \pi_{\mathrm{exp}}$ [21,24]:

$$C_{\mathrm{op}} = \sum_i c_i^{\mathrm{om}}\, S_i + \sum_t \left[\pi_{\mathrm{imp}}(t)\, P_{\mathrm{grid}}^{\mathrm{imp}}(t) - \pi_{\mathrm{exp}}(t)\, P_{\mathrm{grid}}^{\mathrm{exp}}(t)\right] \Delta t \tag{33}$$

The net present cost and annual-equivalent cost are [19,22]:

$$\mathrm{NPC} = C_{\mathrm{cap}} + \sum_i C_{\mathrm{rep},i} + \sum_{y=1}^{N} \frac{C_{\mathrm{op}}}{(1+d)^y}, \qquad C_{\mathrm{ann}} = \mathrm{NPC} \cdot \mathrm{CRF} \tag{34}$$

The levelized cost of hydrogen is calculated as the annualized cost per unit of hydrogen delivered [1,3]:

$$\mathrm{LCOH} = \frac{C_{\mathrm{ann}}}{M_{\mathrm{H_2}}^{\mathrm{yr}}} \tag{35}$$

The renewable fraction measures renewable self-supply relative to grid import [21]:

$$f_{\mathrm{RE}} = 1 - \frac{\sum_t P_{\mathrm{grid}}^{\mathrm{imp}}(t)\,\Delta t}{\sum_t \left(P_{\mathrm{load}}(t) + P_{\mathrm{el}}(t) + P_c(t)\right)\Delta t} \tag{36}$$

Equation (36) is an hourly, import-based metric: every kWh imported, including grid electricity used by the electrolyzer for reserve recovery, reduces f_{RE}, whereas exported electricity is not credited. Battery losses are covered by renewable generation, because the battery is charged only from on-site surplus. Since part of the hydrogen is produced with imported electricity, a hydrogen-specific renewable share is also reported,

$$f_{\mathrm{H_2}} = 1 - \frac{\sum_t P_{\mathrm{grid}}^{\mathrm{imp}}(t)\,\dfrac{P_{\mathrm{el}}(t) + P_c(t)}{P_{\mathrm{load}}(t) + P_{\mathrm{el}}(t) + P_c(t)}\,\Delta t}{\sum_t \left(P_{\mathrm{el}}(t) + P_c(t)\right)\Delta t} \tag{36a}$$

Hydrogen supply reliability is measured by the loss-of-supply probability [20]:

$$\mathrm{LPSP}_{\mathrm{H_2}} = \frac{\sum_t \max\left(0,\ \dot{m}_{\mathrm{H_2}}^{\mathrm{dem}}(t) - \dot{m}_{\mathrm{H_2}}^{\mathrm{disp}}(t)\right)\Delta t}{\sum_t \dot{m}_{\mathrm{H_2}}^{\mathrm{dem}}(t)\,\Delta t} \tag{37}$$

Equations (1)–(37) define the plant model dispatched by the energy management strategy and evaluated within the sizing procedure of Section 2.11. The principal operating and techno-economic inputs are consolidated in Table 3; demonstrator values in Table 2 are used as technical references where applicable. In which hourly imports are attributed pro rata to electrolysis and compression. In this paper, renewable hydrogen denotes station operation that satisfies $f_{\mathrm{RE}} \geq 0.9$; the fraction $1 - f_{\mathrm{H_2}}$ of the hydrogen mass, about 10% in the optimal designs (Tables 4 and 5), is attributable to grid electricity and would not qualify as renewable under hourly-matching criteria such as those of the EU delegated act for renewable fuels of non-biological origin [42], given the low renewable share of the Tunisian grid.

Table 3. Base-case techno-economic and operating assumptions.

Parameter	Base-Case Value	Source or Interpretation
Meteorological period	2015–2025; hourly; 96,432 steps/site	ERA5-Land framework [43]; common multi-site record
Hydrogen dispensing duty	100 kg H_2/day	Representative HRS duty; comparable station scales discussed in [10–13]
Renewable fraction	≥90%	Design requirement used for the base case
Hydrogen LPSP	≤2%	Reliability constraint; zero loss in all base-case optima (Table 5)
Project lifetime	25 years	Economic analysis assumption
Real discount rate	8%	Base-case economic assumption
Battery cost	300 USD/kWh	Base case; sensitivity range 40–300 USD/kWh
Grid import tariff	0.12 USD/kWh	Flat tariff; 0.30 and 0.50 USD/kWh tested (Section 3.7)
Grid export tariff	0.04 USD/kWh	No export and 30% cap tested (Section 3.7)
PEM specific electricity use	55 kWh/kg H_2 (range 50–55)	Literature-based range [3,5]
Fuel-cell rated efficiency	57%	MINCATEC technical anchor, Table 2
Battery cycle anchor	6000 cycles at 80% DoD	MINCATEC technical anchor, Table 2
PV CAPEX	800 USD/kW	Base-case model input; constant-USD planning assumption
Wind CAPEX	1300 USD/kW	Base-case model input; constant-USD planning assumption
PEM electrolyzer CAPEX	1000 USD/kW	Base-case model input; constant-USD planning assumption
Compressed-H_2 storage CAPEX	500 USD/kg H_2	Base-case model input for compressed-gas storage
Fixed O&M	3% of installed CAPEX/year	Base-case annual O&M assumption
Cost basis	Constant USD	Planning-level scenario inputs; not vendor quotations
Electrolyzer balance of plant	455 USD/kW	Rectifier, water treatment and gas conditioning
Electrolyzer stack	80,000 h; 40% of CAPEX	Replacement interval and cost share; Equation (32)
Compressor	4600 USD/kW; 15 years	Three stages, 50 to 900 bar, $\eta_{\mathrm{is}} = 0.55$, $w_c = 2.11$ kWh/kg

Fuel cell	2000 USD/kW; 20,000 h	$P_{fc}^{min} = 0.1\,P_{fc}^{r}$; stack share 60%
Battery operation	SOC 0.2–1.0; reserve 0.3	0.5 C; $\eta_{ch} = \eta_{dis} = 0.95$; calendar life 15 years
Wind turbine	80 m hub; $\alpha = 1/7$	Generic curve; cut-in, rated and cut-out speeds 3, 11.5 and 25 m/s
PV array	$\eta_{dr} = 0.86$; NOCT 45 °C	$\gamma_P = -0.4$ %/K; horizontal irradiance (conservative)
Hydrogen reserve	$H = 12$ h	$m_{st}^{min} = 0.1\,m_{st}^{max}$; Equation (39)
Station auxiliary load	2 kW + 0.6 kWh/kg	Dispensing and pre-cooling
Grid connection	2 MW PCC	Not binding in the base case

Table 4. Least-cost designs by site.

Site	PV [kWp]	Wind [kW]	Battery [kWh]	Electrolyzer [kW]	Comp. [kW]	Fuel Cell [kW]	H_2 Storage [kg]	CAPEX [M$]	LCOH [USD/kg]	f_{RE}
Bizerte	760	666	0	360	20	-	281	2.23	**7.52**	0.90
Gabès	1074	452	80	415	20	-	227	2.28	7.88	0.91
Ben Guerdane	1093	512	-	419	20	-	255	2.37	8.11	0.90
Sousse	2159	-	129	567	26	-	148	2.79	**9.00**	0.90

Table 5. Base-case reliability, hydrogen reserve and PSO repeatability.

Indicator	Bizerte	Gabès	Ben Guerdane	Sousse
LPSP of the Table 4 design (%)	0.000	0.000	0.000	0.000
LPSP of the re-optimized base-case design (best of ten runs) [1] (%)	0.000	0.000	0.000	0.000
Minimum stored H_2 (kg)	75	71	69	63
Reserve level m_{res}/residual inventory m_{st}^{min} (kg) [2]	75.5/25.5	70.8/20.8	68.6/18.6	63.2/13.2
Reserve recovery (h/year)	669	579	498	376
f_{H_2} (–)	0.900	0.900	0.900	0.901
Grid import (GWh/year)	0.21	0.21	0.21	0.21
Grid export (GWh/year)	0.99	0.70	0.75	1.06
Electrolyzer operation (h/year)	7519	7201	6356	4372
Electrolyzer starts (1/year)	399	533	608	591
Stack replacement interval (years)	10.6	11.1	12.6	18.3
Best LCOH of ten runs (USD/kg)	7.53	7.92	8.08	8.97
Standard deviation of LCOH (USD/kg)	0.0002	0.0008	0.0045	0.0126
Capacity CV, PV/wind/electrolyzer/storage (%)	1.4/1.7/0.6/1.4	1.4/3.0/1.1/1.4	3.2/7.9/1.9/4.8	1.1/–/0.8/1.1

[1] Best of the ten independent base-case PSO runs of Section 3.6 (capacities in the 0.90 rows of Table 6; LCOH in the first row of Table 7). The operating indicators, from the minimum stored H_2 to the stack replacement interval, refer to these designs, and the last three rows summarize the ten runs. The scenario re-optimizations, whose LPSP values are given in Table 7, are not included. [2] Reserve level of Equation (39), $m_{res} = m_{st}^{min} + 50$ kg (12 h of the 4.17 kg/h base-case demand), with $m_{st}^{min} = 0.1\,m_{st}^{max}$ (Equation (22)); the stored mass may fall temporarily below m_{res}, which triggers reserve recovery (Section 2.11.1).

Table 6. Design versus renewable fraction.

Site	f_{RE}^{min}	PV (kWp)	Wind (kW)	Battery (kWh)	Electrolyzer (kW)	H_2 Storage (kg)	Import (GWh/year)	LCOH (USD/kg)
Bizerte	none (0.58)	387	438	0	230	100	0.88	7.13
	0.80	591	661	0	311	157	0.43	7.29
	0.90	745	716	0	359	255	0.21	7.53
	0.95	854	787	0	380	342	0.11	7.81
Gabès	none (0.52)	486	288	0	230	100	1.02	7.42
	0.80	814	494	0	348	144	0.43	7.67
	0.90	1003	526	0	407	208	0.21	7.92
	0.95	1109	631	0	425	289	0.11	8.27

Ben Guerdane	none (0.48)	496	246	0	230	100	1.10	7.54
	0.80	1063	285	0	425	123	0.43	7.80
	0.90	1204	414	0	457	186	0.21	8.08
	0.95	1446	483	0	487	252	0.11	8.54
Sousse	none (0.35)	616	0	0	230	100	1.39	7.80
	0.80	1582	0	0	512	119	0.43	8.33
	0.90	2061	0	61	590	132	0.21	8.97
	0.95	2419	0	76	670	150	0.11	9.66

Table 7. Scenario results (LCOH of the design re-optimized for each scenario, USD/kg).

Scenario	Bizerte	Gabès	Ben Guerdane	Sousse	Main Design Response
Base case (best of ten runs)	7.53	7.92	8.08	8.97	Table 4 structure; no fuel cell
Wind speed +10%	6.73	7.19	7.56	8.97	More wind; Sousse unchanged
Wind speed +20%	5.85	6.44	6.88	8.94	Wind up to 1500 kW; 20 kW at Sousse
No export	8.19	8.49	8.73	9.91	0.40–0.77 GWh/year curtailed; larger tanks
Export ≤ 30% of production	7.60	7.93	8.10	9.15	Small curtailment
Import ≤ 100 kW	7.47	7.87	8.10	8.99	LPSP 0.15–1.02%
Unrestricted fuel cell dispatch	7.53	7.92	8.08	8.97	Fuel cell 0 kW at all sites
Import tariff 0.30 USD/kWh	8.32	8.79	9.03	10.01	Fuel cell 0 kW; f_{RE} 0.90–0.96
Import tariff 0.50 USD/kWh	8.68	9.23	9.55	10.74	Fuel cell 0 kW; f_{RE} 0.96–0.98
Outages, 5% of hours (6 h events)	7.58	7.95	8.11	9.00	Fuel cell 0 kW; LPSP 0.33–0.55%
Outages, 2% of hours (48 h events)	7.54	7.93	8.09	8.98	Fuel cell 0 kW; LPSP 0.16–0.25%
Same, fuel cell at 1000 USD/kW	7.54	7.93	8.09	8.98	Fuel cell 0 kW
Off-grid operation	9.42	9.82	10.31	12.38	Fuel cell 5 kW at Bizerte only; LPSP 2.0%
Diurnal demand profile	7.54	7.93	8.09	8.99	Tank up to +11%
Stochastic demand profile	7.63	8.02	8.20	9.16	Tank +20–48%
Demand 50 kg/day	7.72	8.11	8.26	9.13	Proportionally scaled design
Demand 200 kg/day	7.49	7.89	8.05	8.93	Proportionally scaled design
Part-load SEC, Equation (17a)	7.48	7.87	8.03	8.91	Mean SEC 54.4–54.5 kWh/kg
Degradation D1	8.39	8.99	9.40	10.65	Stack life 3.9–4.7 years; more wind
Degradation D2 (stress case)	11.61	11.04	12.15	13.66	MWh-scale batteries; about 20 starts per year

2.11. Energy Management and Optimal Sizing

The design problem is solved in two nested layers. For each candidate set of component ratings, an inner operational layer simulates hourly dispatch over the full 2015–2025 record using the rule-based EMS described in Section 2.11.1. An outer planning layer then applies PSO to search for the least-cost design that satisfies the reliability and renewable-fraction constraints. Because the economic indicators depend on the complete operating trajectory, every candidate proposed by PSO is evaluated through a full 96,432-h simulation.

2.11.1. Reserve-Aware Rule-Based Energy Management Strategy

At each time step, the EMS follows a fixed dispatch priority designed to maximize renewable self-supply while preserving hydrogen availability for dispensing [16,20]. Net renewable power after conversion is $P_{net}(t) = P_{PV}(t) + P_{WT}^{\rho}(t)$, and the instantaneous balance closes through Equation (27). The priority order is:

1. Serve the station electrical demand using renewable generation first, followed by the battery, the fuel cell when its hydrogen reserve permits, and finally the grid.
2. Use renewable surplus for electrolysis within the admissible turndown range and supply the compressor, provided the battery remains above its reserve.
3. Charge the battery with any remaining surplus and export residual energy within the point-of-common-coupling limit.

4. During renewable deficits, discharge the battery down to its reserve and import the remaining requirement from the grid. The fuel cell is dispatched only when stored hydrogen exceeds its reserve and either the import price exceeds the threshold of Equation (39a) or the grid is unavailable.

To prevent excessive depletion of the two storage buffers, the EMS imposes explicit operating reserves. The battery reserve is defined by:

$$\mathrm{SOC}(t) \geq \mathrm{SOC}_{\mathrm{res}} \tag{38}$$

The hydrogen reserve level $m_{\mathrm{res}}(t)$ is the inventory that the high-pressure tank should retain to cover the expected dispensing over a look-ahead horizon H, in addition to the residual inventory $m_{\mathrm{st}}^{\min}$ of Equation (22):

$$m_{\mathrm{res}}(t) = m_{\mathrm{st}}^{\min} + \sum_{\tau=t+1}^{t+H} \dot{m}_{\mathrm{H_2}}^{\mathrm{dem}}(\tau)\,\Delta t \tag{39}$$

Equation (39) is used as a soft operating target rather than as a hard constraint. The reserve test is evaluated at every hourly time step, after dispensing (Algorithm 1), and the condition $m_{\mathrm{st}}(t) < m_{\mathrm{res}}(t)$ triggers reserve recovery: the electrolyzer set-point is increased toward rated power. Grid electricity is used when renewable generation is insufficient, which protects dispensing reliability during multi-day low-resource periods. The reserve test appears in both branches of Figure 2 because it plays different roles: in surplus hours it allows the electrolyzer to top up to rated power, whereas in deficit hours it decides whether the electrolyzer stays on with grid supply or is switched off. The reserve horizon is $H = 12$ h. Because recovery starts only after the threshold has been crossed, the stored mass may fall temporarily below $m_{\mathrm{res}}(t)$. For the hydrogen inventory, only the physical bounds of Equation (22) are enforced at every time step: dispensing is limited to the inventory above $m_{\mathrm{st}}^{\min}$, and any demand left unserved enters the LPSP of Equation (37). In the base case, grid import is not restricted, so the electrolyzer can always be raised to its rated power, which exceeds the power required by the mean demand (Section 3.2); the minimum stored mass therefore differs by less than 1 kg from the reserve level of the corresponding design (Table 5). When grid-fed recovery is restricted, as with the 100 kW import cap of Section 3.7, the stored mass can remain below $m_{\mathrm{res}}(t)$ during long low-resource periods, and the inventory above $m_{\mathrm{st}}^{\min}$ can be exhausted, which produces the non-zero LPSP of that scenario in Table 7.

The fuel cell price threshold values the stored hydrogen at the export price of the renewable electricity used to produce and compress it,

$$\pi_{\mathrm{fc}}^{\mathrm{th}} = \frac{\pi_{\mathrm{exp}}(\mathrm{SEC} + w_c)}{\eta_{\mathrm{fc}}\,\mathrm{LHV}_{\mathrm{H_2}}} \tag{39a}$$

Which gives $\pi_{\mathrm{fc}}^{\mathrm{th}} = 0.12$ USD/kWh for the base-case tariffs. Under the flat import tariff of 0.12 USD/kWh, the rule therefore never triggers economic fuel cell dispatch, and the fuel cell can operate only during grid outages. To verify that the zero fuel cell capacity of Section 3 is not an artefact of this rule, the optimization was repeated with an unrestricted rule that dispatches the fuel cell whenever a deficit remains after the battery and the hydrogen reserve permits (Section 3.7). Figure 2 and Algorithm 1 summarize the dispatch logic.

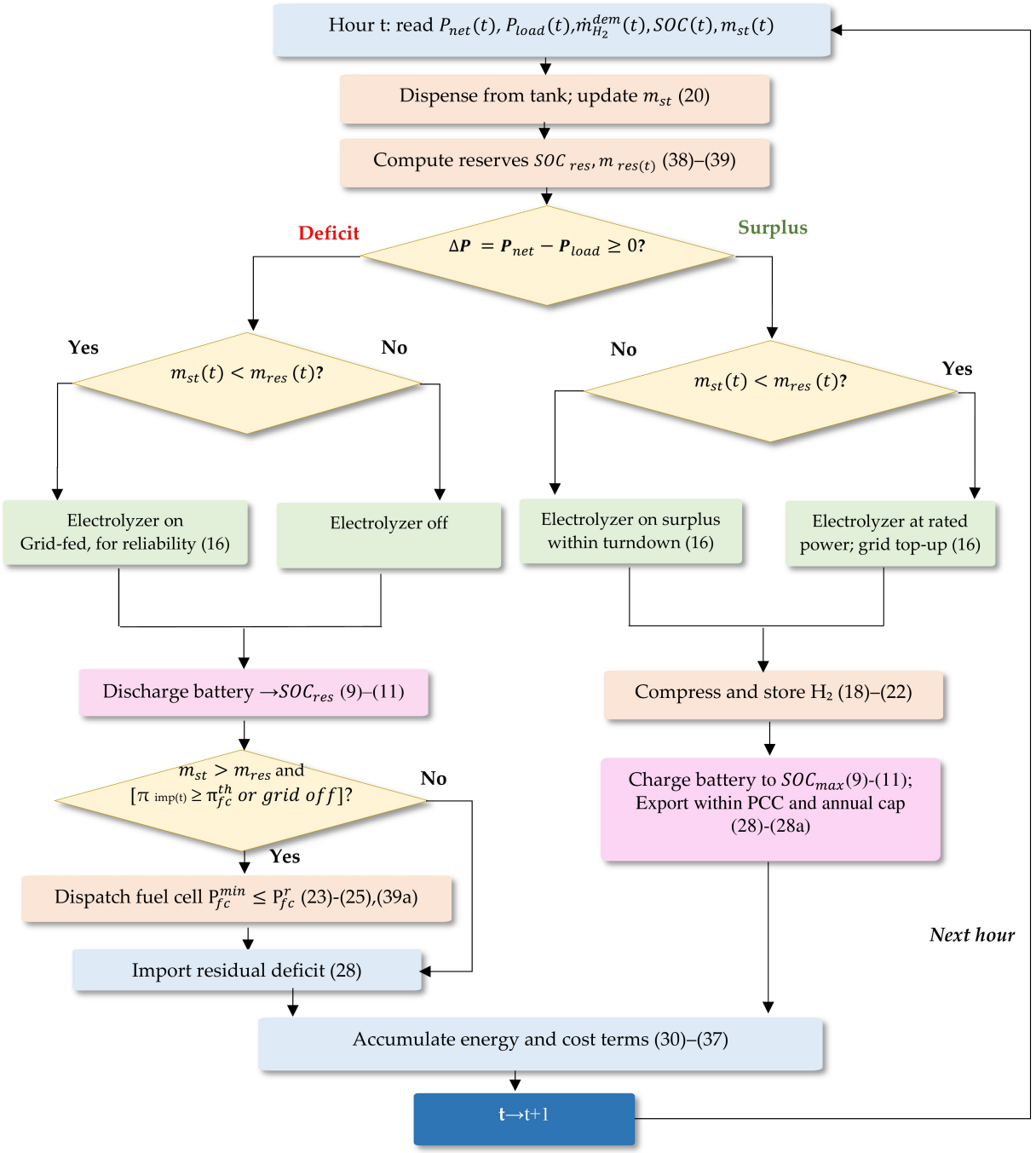

Figure 2. Reserve-aware rule-based energy management strategy.

Algorithm 1. Hourly energy management strategy (executed for each t).
Inputs: $P_{\text{net}}(t)$, $P_{\text{load}}(t)$, $\dot{m}_{\text{H}_2}^{\text{disp}}(t)$, states $\text{SOC}(t)$, $m_{\text{st}}(t)$; ratings $\mathbf{x}$. 1. Meet dispensing $\dot{m}_{\text{H}_2}^{\text{disp}}(t)$ from the tank; update m_{st} (20). 2. Compute reserves SOC_{res}, $m_{\text{res}}(t)$ from (38) and (39). 3. $\Delta P \leftarrow P_{\text{net}}(t) - P_{\text{load}}(t)$. 4. **if** $\Delta P \geq 0$ (surplus): a. **if** $m_{\text{st}}(t) < m_{\text{res}}(t)$: run electrolyzer at $\min\left(P_{\text{el}}^{\text{rated}}, \Delta P + P_{\text{grid}}^{\text{avail}}\right)$ to refill; **else** run electrolyzer at $\min\left(P_{\text{el}}^{\text{rated}}, \Delta P\right)$ within turndown (16). b. compress produced H_2 (18)–(19); update m_{st} (20)–(22). c. route remaining surplus to battery up to SOC_{max} (9)–(11); export the rest to grid (28). 5. **else** (deficit): a. **if** $m_{\text{st}}(t) < m_{\text{res}}(t)$: keep electrolyzer on (grid-fed) to protect reliability. b. discharge battery down to SOC_{res} (9)–(11); then dispatch fuel cell if $m_{\text{st}}(t) > m_{\text{res}}(t)$ and $\pi_{\text{imp}}(t) \geq \pi_{\text{fc}}^{\text{th}}$ (39a) or the grid is unavailable, with $P_{\text{fc}} \geq P_{\text{fc}}^{\text{min}}$ (23)–(25). c. import the residual deficit from the grid (28). 6. Accumulate energy and cost terms (30)–(37).

2.11.2. Optimal Sizing by Particle Swarm Optimization

Decision variables. The outer layer optimizes the seven component ratings collected in the design vector:

$$\mathbf{x} = \left[P_{\mathrm{PV}}^{r}, P_{\mathrm{WT}}^{r}, E_{b}^{\mathrm{cap}}, P_{\mathrm{el}}^{r}, P_{c}^{r}, P_{\mathrm{fc}}^{r}, m_{\mathrm{st}}^{\max} \right] \tag{40}$$

Objective. The design minimizes the LCOH defined by Equation (35) under the dispatch generated by the EMS:

$$\mathbf{x}_{\min} \le \mathbf{x} \le \mathbf{x}_{\max} \tag{41}$$

Constraints. Feasible designs must satisfy the hydrogen-supply reliability and renewable-fraction requirements:

$$\mathrm{LPSP}_{\mathrm{H_2}}(\mathbf{x}) \le \varepsilon_{\mathrm{H_2}} \tag{42}$$

$$f_{\mathrm{RE}}(\mathbf{x}) \ge f_{\mathrm{RE}}^{\min} \tag{43}$$

The component ratings are also restricted by the following technology bounds:

$$\mathbf{x}_{\min} \le \mathbf{x} \le \mathbf{x}_{\max} \tag{44}$$

Constraint handling. The inequality constraints in Equations (42) and (43) are enforced through a quadratic exterior penalty added to the objective [29]:

$$F(\mathbf{x}) = \mathrm{LCOH}(\mathbf{x}) + \sum_{j} \mu_j \left[\max\left(0, g_j(\mathbf{x})\right)\right]^2 \tag{45}$$

where $g_j \le 0$ are the normalized forms of (42) and (43) and μ_j are penalty weights.

Swarm dynamics. Each particle i carries a position $\mathbf{x}_i$ (a candidate design) and velocity $\mathbf{v}_i$, and the velocity is updated toward its personal best $\mathbf{p}_i$ and global best $\mathbf{g}$ [29,30]:

$$\mathrm{v}_i^{k+1} = w^k \mathrm{v}_i^k + c_1 r_1 \left(\mathrm{p}_i - \mathrm{x}_i^k\right) + c_2 r_2 \left(\mathrm{g} - \mathrm{x}_i^k\right) \tag{46}$$

$$\mathrm{x}_i^{k+1} = \mathrm{x}_i^k + \mathrm{v}_i^{k+1} \tag{47}$$

where $r_1, r_2 \sim \mathcal{U}(0,1)$ are independent random variables and c_1, c_2 are the cognitive and social coefficients. The inertia weight decreases linearly over the $k_{\max}$ iterations to balance exploration and exploitation [30]:

$$w^k = w_{\max} - (w_{\max} - w_{\min}) \frac{k}{k_{\max}} \tag{48}$$

PSO implementation settings. The implementation uses 28 particles. The cognitive and social coefficients are both set to 1.5, and the inertia weight decreases linearly from 0.90 to 0.40 according to Equation (48). These values follow standard recommendations: an inertia weight decreasing linearly from 0.9 to 0.4 [44,45] and equal acceleration coefficients within the range of 1.49–2.0 associated with stable convergence [46]. The swarm of four particles per decision variable balances exploration against the cost of one 96,432 h simulation per evaluation. The search stops after $k_{\max} = 150$ iterations, or earlier if the global best improves by less than 10^{-5} USD/kg over 30 consecutive iterations, and velocities are limited to 20% of the search range. The bounds of Equation (44) are 0–3000 kWp for PV, 0–1500 kW for wind, 0–4000 kWh for the battery, 230–900 kW for the electrolyzer, 20–60 kW for the compressor, 0–300 kW for the fuel cell, and 100–700 kg for storage. Ratings below a minimum unit size (10 kW for PV and wind, 5 kWh for the battery and 2 kW for the fuel cell) are set to zero, which allows a technology to leave the design, and the penalty weights μ_j include a fixed offset so that any infeasible design ranks below all

feasible designs. Ten independent runs with different random seeds were performed for each site, and alternative settings were tested at Gabès (Section 3.6).

In the scenario re-optimizations of Sections 3.5–3.9, one particle is initialized at the base-case optimum of the site, and the iteration limit is 100. Particles are initialized uniformly within the common technology search box and are clamped to the admissible bounds after each update. Each fitness evaluation replays the complete 96,432-h dispatch record. A dense-grid benchmark used in the project implementation agreed with the best PSO solution to within 1%, which is treated as a numerical consistency check rather than a proof of global optimality.

Positions are clamped to the bounds (44) after each update. The procedure, comprising swarm initialization, per-particle 11-year EMS evaluation, personal- and global-best updates, and velocity/position updates until convergence, is summarized in Figure 3. Because each fitness evaluation is a full multi-year simulation, the objective landscape is non-convex and non-smooth, which is well suited to population-based metaheuristics such as PSO [29,30]. The search stops when the global-best fitness remains unchanged for a prescribed number of iterations or when $k_{\max}$ is reached.

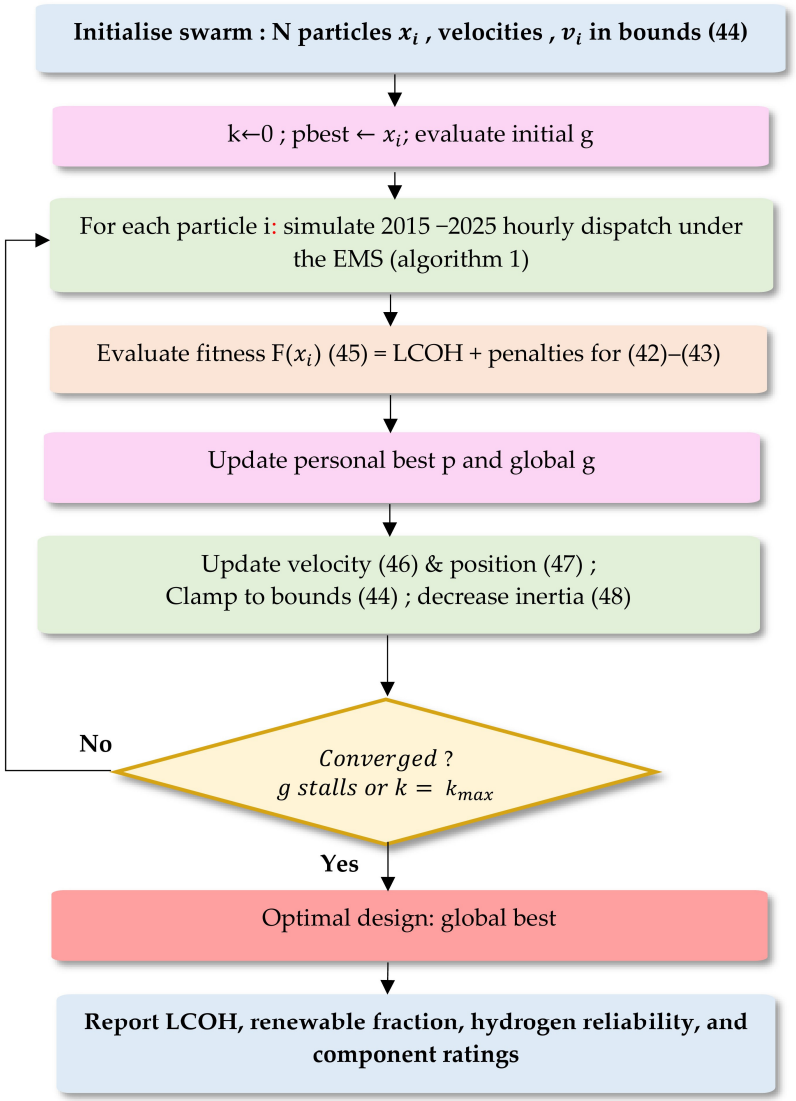

Figure 3. Nested PSO procedure for least-cost sizing.

2.12. Data Quality, Base-Case Assumptions, and Scope

Meteorological data. ERA5-Land is a gridded reanalysis product rather than an in-situ measurement record [43]. It is used here to obtain a spatially consistent hourly dataset for all four sites. Surface solar radiation is converted only after checking the ERA5-Land accumulation convention, and the 10 m wind speed is extrapolated to hub height using Equation (5). The parent ERA5 reanalysis and the ERA5-Land dataset are documented in [43,47]. Completeness was verified for every variable used (t2m, ssrd, u10, v10 and sp): each site contains 96,432 consecutive hourly records, with no missing values and no missing or duplicated timestamps, so no gap filling was required. The radiation fields are supplied as hourly de-accumulated values; the only correction concerns 419–513 small negative values per site (below 0.002 W/m^2, all in night or twilight hours), which were set to zero.

Wind-data scope. A recent independent study reported systematic under-representation of 10 m wind speed in ERA5-Land relative to ERA5 in several regions [48]. An independently validated correction factor for the four Tunisian sites is not available in the present dataset, and independent mast or LiDAR measurements were not accessible to the authors, so no site-specific correction is applied in the base case. Instead, the sensitivity of the conclusions to a systematic low bias is tested by scaling all hub-height wind speeds by 1.10 and 1.20 and re-optimizing every site (Section 3.7). Reanalyses are known to underestimate strong winds, for instance offshore in ERA5 [49], although ERA5 remains among the best reanalyses for near-surface winds [50]; the two factors therefore bracket a plausible common bias rather than a validated correction. Wind-sensitive outputs are therefore interpreted as comparative scenario results rather than investment-grade wind-resource estimates. The use of one data product and one processing chain preserves internal consistency among the four sites, but it does not remove the possibility of a common reanalysis bias.

Economic and operating assumptions. Table 3 consolidates the principal operating and techno-economic inputs used in the base case. The unit-cost values are treated as constant scenario assumptions for comparative planning rather than as 2026 vendor quotations. Component-specific costs enter the annualized cost relations in Equations (30)–(34), while the MINCATEC prices in Table 2 are retained only as demonstrator-scale technology anchors. In this paper, renewable hydrogen denotes station operation satisfying the imposed renewable-fraction constraint; limited grid electricity may still be used for reserve recovery during low-resource periods.

Implementation consistency and interpretation. The same optimization formulation, component bounds, constraint treatment, dispatch priorities, inertia law, and stopping logic are applied to all four sites. The study does not claim superiority of PSO over alternative optimizers, nor experimental validation of the optimized station. The MINCATEC installation is used only as a physical parameter anchor because its storage technology and control architecture differ from the simulated grid-connected configuration.

3. Results

The framework was applied to the four coastal sites using the complete 2015–2025 ERA5-Land record (96,432 hourly steps per site). Unless stated otherwise, the station dispenses 100 kg H_2/day. Each candidate design must keep the hydrogen loss-of-supply probability at or below 2% and the renewable fraction at or above 90%, while minimising LCOH. Key base-case assumptions are consolidated in Table 3, and demonstrator-based technical anchors are summarized in Table 2. An 8% real discount rate and a 25-year project lifetime are used throughout. Sections 3.6–3.9 test the robustness of these results with re-optimized designs.

3.1. Resource Characterization

The four sites exhibit distinct solar and wind resource profiles (Figure 4). Mean annual global horizontal irradiation increases from 1793 kWh/m²/year at Bizerte to 1875 kWh/m²/year at Sousse, 2006 kWh/m²/year at Gabès, and 2039 kWh/m²/year at Ben Guerdane. The wind resource shows the opposite tendency: the Weibull scale parameter is highest at Bizerte ($c = 7.88$ m/s, $k = 2.09$) and lowest at Sousse ($c = 5.34$ m/s, $k = 2.07$), with Gabès ($c = 7.14$ m/s, $k = 2.28$) and Ben Guerdane ($c = 6.93$ m/s, $k = 2.16$) between these values. The seasonal profiles also show that stronger winter winds partly compensate for lower solar availability, consistent with complementarity reported for North African sites [34]. At 80 m, the generic turbine reaches capacity factors of 29.7%, 23.1%, 21.7% and 10.7% at Bizerte, Gabès, Ben Guerdane and Sousse, and the specific PV yields are 1402–1560 kWh/kWp per year.

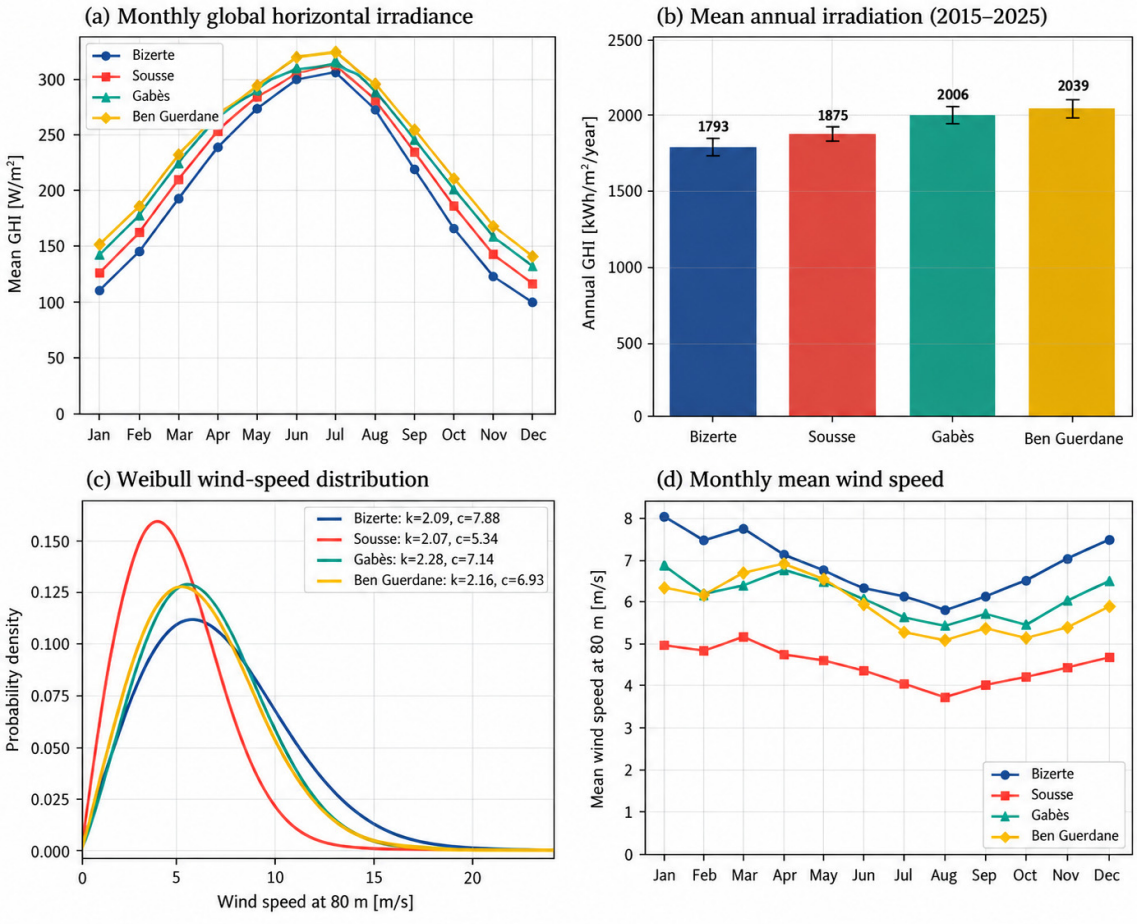

Figure 4. Solar and wind resources at the four Tunisian coastal sites.

3.2. Optimal Designs Across the Four Sites

Table 4 and Figure 5 summarize the least-cost designs. Three qualitative patterns emerge consistently under the common optimization setup:

- **Fuel-cell capacity is not selected under the base-case grid and cost assumptions.** With grid access, importing electricity during deficits is less costly than storing hydrogen and reconverting it through the electrolyzer-fuel-cell pathway, whose round-trip efficiency is about 33% including compression. The optimizer therefore assigns zero fuel-cell capacity at all four sites in this scenario. This outcome is not imposed by the dispatch rule: with unrestricted fuel cell dispatch, the optimizer still selects zero capacity at all four sites (Section 3.7).

- **Wind capacity is selected only at sites with a sufficiently strong resource.** The optimum includes 666 kW at Bizerte, 512 kW at Ben Guerdane, and 452 kW at Gabès, but no wind capacity at Sousse. The Sousse design instead relies on a 2.16 MWp PV array. Wind enters the design at hub-height capacity factors of 21.7% and above, but not at 10.7% (Sousse).
- **Battery capacity remains limited at the assumed 300 USD/kWh.** Optimal battery capacity ranges from 0 kWh at Bizerte and Ben Guerdane to approximately 130 kWh at Sousse, which is small relative to installed renewable capacity. This result is specific to the base-case battery price and grid conditions; short-term flexibility is supplied mainly through electrolyzer modulation, hydrogen storage, and grid exchange. The LCOH is nearly flat in this range: across the ten repeated runs at Sousse, the battery varied between 0 and 63 kWh with LCOH differences below 0.4% (Section 3.6).

The electrolyzer rating ranges from 360 to 567 kW, above the approximately 229 kW mean electrical power associated with 100 kg/day of hydrogen production. This additional capacity allows the system to absorb high renewable output during favorable hours. Compressor capacity varies from 20 to 26 kW according to the peak hydrogen production rate. The hydrogen buffer ranges from 148 to 281 kg, equivalent to approximately 1.5–2.8 days of demand, and provides multi-day flexibility during low-resource periods.

Table 5 reports the base-case reliability and grid indicators: no hydrogen demand is left unserved at any site, both for the designs of Table 4 and for the re-optimized base-case designs, i.e., the best of the ten independent PSO runs of Section 3.6 (capacities in the 0.90 rows of Table 6; LCOH in the first row of Table 7). The operating indicators of Table 5 refer to these re-optimized designs. Their minimum stored mass (63–75 kg) differs by less than 1 kg from the corresponding reserve level m_{res} of Equation (39) (63.2–75.5 kg) and remains about 50 kg, i.e., the 12 h demand reserve, above the residual inventory $m_{\mathrm{st}}^{\mathrm{min}}$ (13.2–25.5 kg). The tank is therefore drawn down to the reserve threshold during low-resource periods, which triggers reserve recovery in 376–669 h/year, but the inventory available for dispensing is never exhausted. The scenario re-optimizations of Sections 3.7 and 3.8 are reported separately in Table 7; their non-zero LPSP values (0.15–2.0%) belong to designs re-optimized with restricted grid access (100 kW import cap, grid outages and off-grid operation) and remain within the 2% limit.

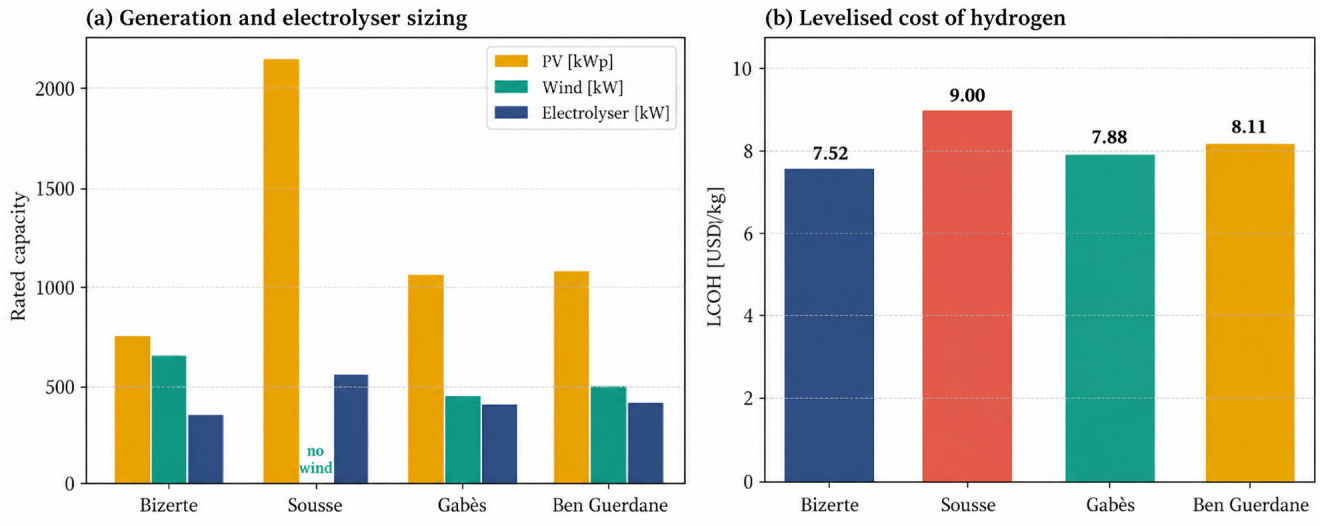

Figure 5. Optimal component sizing and LCOH across sites.

3.3. Cost Structure

The LCOH decomposition in Figure 6 explains the differences among sites. The electrolyzer contribution remains within approximately 2.1–3.3 USD/kg, while the generation mix accounts for most of the site-to-site variation. At Bizerte, the cost is distributed between wind (3.03 USD/kg) and PV (2.04 USD/kg). At Sousse, the PV contribution reaches 5.78 USD/kg because the 90% renewable-fraction requirement must be met without economically viable wind capacity. Grid exchange produces a small net credit at all sites, from −0.11 to −0.68 USD/kg, because revenue from surplus exports (0.69–1.25 GWh/year) exceeds the cost of the remaining imports under the assumed tariff structure. Because this credit relies on unrestricted export at 0.04 USD/kWh, Section 3.7 re-optimizes the designs without export revenue and with the 30% export cap of Equation (28a).

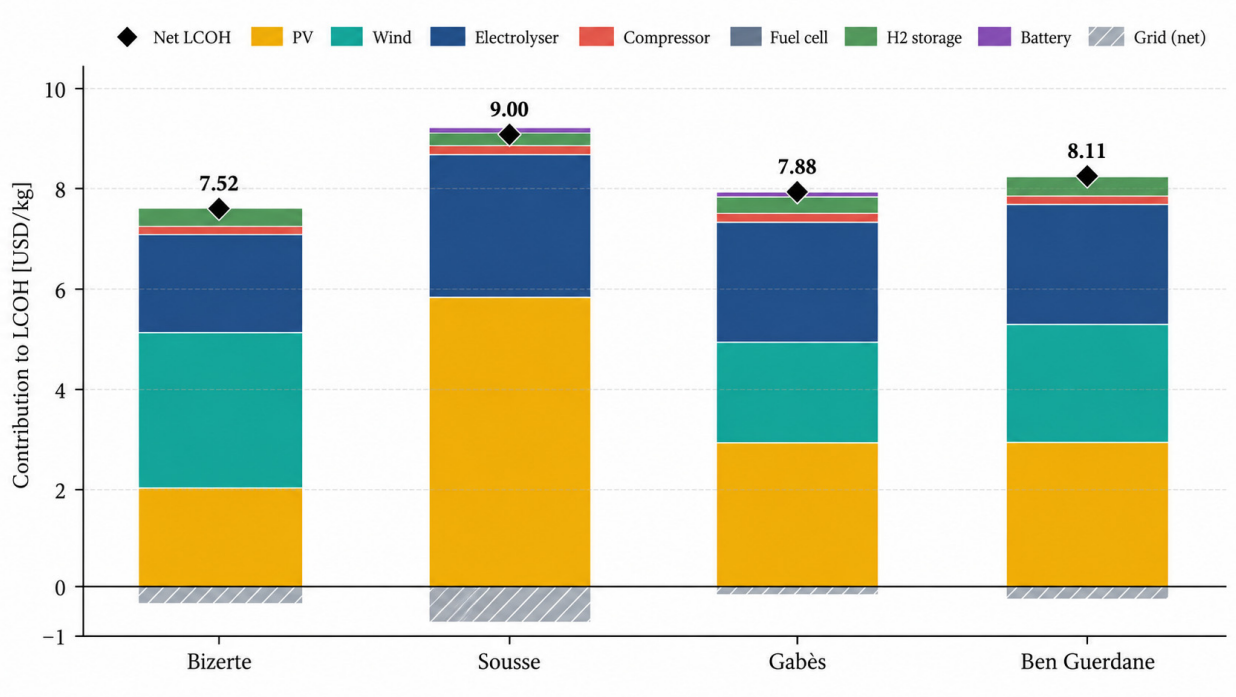

Figure 6. LCOH decomposition by component and net grid credit.

3.4. Operational Behavior

Figure 7 shows a representative 12-day winter operating period for the optimal Gabès design. Electrolyzer power follows the combined PV-wind output and reaches rated power during high-generation intervals. The battery cycles between its reserve floor and full charge, while the hydrogen tank provides the main multi-day buffer. Storage increases during the favorable resource period on days 3–6 and is then drawn down during the lower-resource period on days 9–11. During these hours, grid imports support the reserve-protected electrolyzer and residual electrical demand. The reserve rules therefore maintain hydrogen availability, with zero hydrogen supply loss in the base-case optimal designs (Table 5).

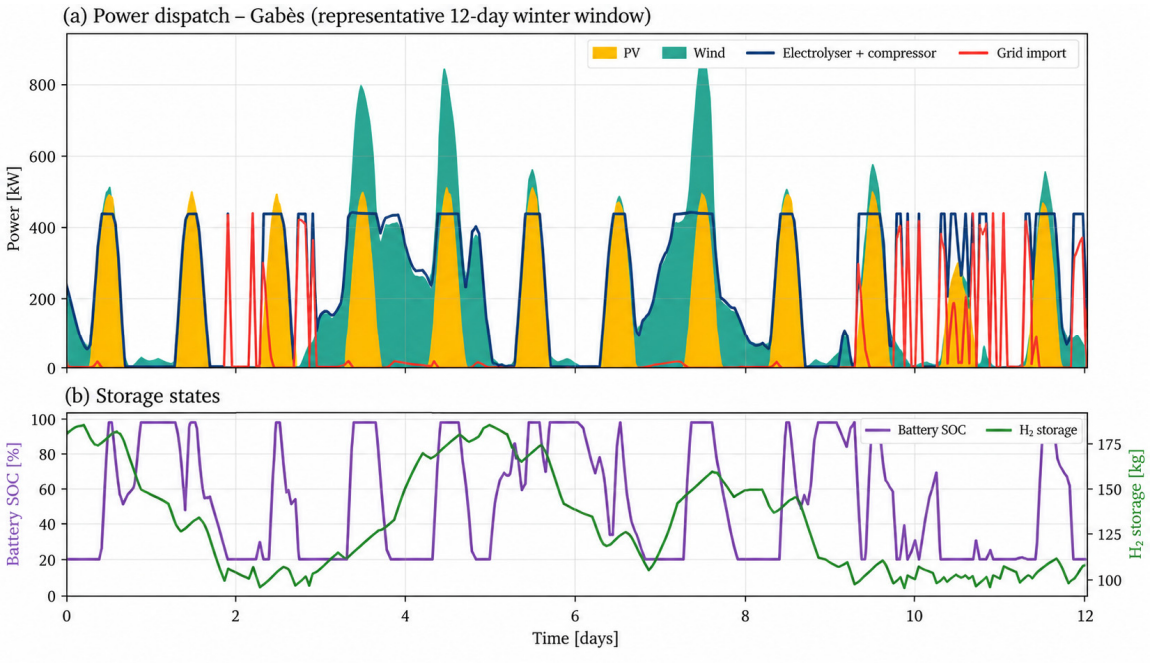

Figure 7. Representative 12-day operation of the optimal Gabès system.

3.5. Sensitivity Analyses

Battery cost. The battery cost was varied from 40 to 300 USD/kWh at all four sites (Figure 8a). At the PV-dominated Sousse site, the optimal battery grows from 61 kWh at 300 USD/kWh to 212 kWh at 150 USD/kWh and 1.44 MWh at 120 USD/kWh, so the 120–150 USD/kWh interval marks its entry threshold. At the three wind sites, the threshold is lower: Ben Guerdane selects 2.77 MWh at 80 USD/kWh, Gabès only 115 kWh at 80 USD/kWh, and Bizerte, whose wind output already covers part of the night, selects no battery above 40 USD/kWh. At 40 USD/kWh, every site installs about 4 MWh, the upper bound of the search space, which replaces part of the electrolyzer oversizing and hydrogen storage (electrolyzer 230–263 kW, tank at its 100 kg lower bound). Battery entry is therefore site-specific and occurs earlier where the solar profile is not complemented by wind, consistent with the context-dependent competition between battery and hydrogen storage reported in [4,33].

Renewable fraction. The renewable fraction constraint was varied from unconstrained cost minimization to 95% at all four sites (Figure 8b and Table 6). Unconstrained designs reach 35–58% renewable supply under the assumed tariffs, with the electrolyzer and the tank at their lower bounds and annual imports of 0.88–1.39 GWh. Raising the target to 90% increases the LCOH by 5.6% at Bizerte, 6.7% at Gabès, 7.1% at Ben Guerdane and 15.0% at Sousse, and a 95% target adds a further 3.7–7.7%. Table 6 shows that the premium is not caused by PV oversizing alone. At Gabès, moving from the unconstrained design to 90% adds 1.40 USD/kg of PV, 1.05 USD/kg of wind and 1.04 USD/kg of electrolyzer cost, partly offset by a 3.18 USD/kg reduction in net grid cost, while storage adds only 0.18 USD/kg and no battery is installed. At Sousse, where wind is excluded, PV dominates the increase (3.91 USD/kg), and the electrolyzer becomes 2.6 times larger than in the unconstrained design. The renewable premium is therefore a site-dependent policy-scenario result rather than a universal cost.

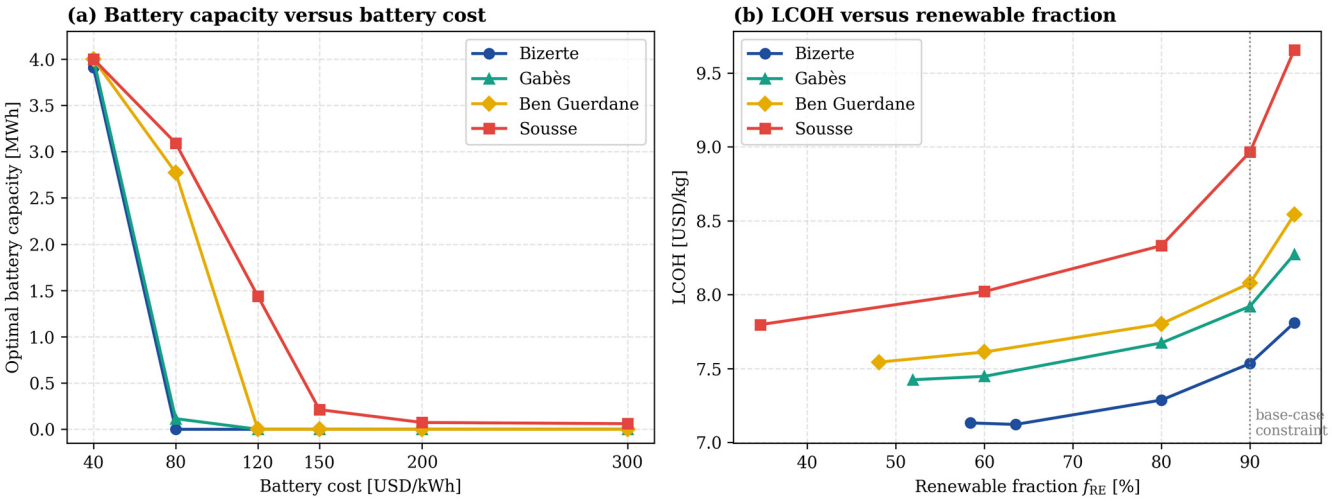

Figure 8. Battery and renewable fraction sensitivity.

3.6. Repeatability of the Optimization

The base-case optimization was repeated ten times per site with independent random seeds (Table 5). The best LCOH values, 7.53, 7.92, 8.08 and 8.97 USD/kg, lie within about 0.5% of the values in Table 4. The best run at each site defines the re-optimized base-case design of Tables 5–7 (0.90 rows of Table 6), which is also the reference for the relative changes reported for the scenario re-optimizations of Sections 3.5, 3.7 and 3.8. The standard deviation across runs is below 0.001 USD/kg at Bizerte and Gabès and 0.005–0.013 USD/kg at Ben Guerdane and Sousse, and the largest spread between runs is 0.37% (Sousse). Capacities vary more than the cost: the coefficient of variation is 1–3% for PV, the electrolyzer and storage, but reaches 7.9% for wind at Ben Guerdane, where PV and wind can be traded against each other at almost constant cost; the small Sousse battery appears in some runs and not in others for the same reason. The reported capacities should therefore be read as representatives of a flat near-optimal region rather than as unique optima. Alternative PSO settings tested at Gabès (40 particles, $c_1 = c_2 = 2.0$, and a constriction-type setting with $c_1 = c_2 = 1.49445$ and $w = 0.7298$) reached the same LCOH within 0.03%, whereas one of two runs with 20 particles converged 0.4% above the best value, which supports the choice of 28 particles.

3.7. Wind Data Bias, Grid Exchange and Fuel Cell Entry

Table 7 summarizes the scenario re-optimizations of Sections 3.7 and 3.8. The site ranking of Table 4 is preserved in every scenario except the D2 degradation stress case. Each entry refers to the design re-optimized under the assumptions of that scenario; the LPSP values given in the last column therefore apply to these scenario designs and are distinct from the zero LPSP of the base-case designs in Table 5.

Wind data bias. Scaling all hub-height wind speeds by 1.10 reduces the LCOH by 10.6% at Bizerte, 9.3% at Gabès and 6.4% at Ben Guerdane, and a factor of 1.20 reduces it by 14.8–22.4%, mainly through larger wind capacities (up to the 1500 kW bound at Bizerte, with exports of 3.7 GWh/year). Sousse is almost unaffected: even with a 20% correction, its capacity factor rises only to 18.0%, and the optimizer installs just 20 kW of wind. A systematic low bias in ERA5-Land would therefore strengthen, not weaken, the conclusion that wind complementarity lowers the cost at the three wind sites, while the absolute LCOH of these sites is conservative.

Export and import restrictions. Without export revenue, 0.40–0.77 GWh/year of surplus electricity is curtailed, the tank grows (for example from 255 to 361 kg at Bizerte), and the LCOH rises by 7.2–10.5% to 8.19–9.91 USD/kg; with the 30% export cap of the Tunisian

self-generation regime, the increase is only 0.2–2.0%. The net grid credit of Section 3.3 is therefore not responsible for the site ordering. Limiting imports to 100 kW changes the LCOH by −0.8% to +0.3%; the slight reduction at Bizerte and Gabès arises because the cap restricts grid-fed reserve recovery, which raises the LPSP to 0.15–1.02% while remaining within the 2% limit. This indicates that the reserve rule is conservative and that a cost-aware recovery policy could lower the LCOH slightly.

Fuel cell entry. The zero fuel cell capacity is robust. With the unrestricted dispatch rule, the optimizer still selects no fuel cell, and the designs and LCOH are identical to the base case, so the result is not induced by the price condition of Equation (39a). Fuel cell capacity also remains zero with import tariffs of 0.30 and 0.50 USD/kWh, which instead raise the voluntary renewable fraction to 0.90–0.98 through additional generation and hydrogen storage; with grid outages covering 5% of the hours in 6 h events or 2% of the hours in 48 h events, even when the fuel cell CAPEX is halved to 1000 USD/kW; and with imports limited to 100 kW. Without backup, dispensing is interrupted only in outage hours, which gives an LPSP of 0.16–0.55%, below the 2% limit, so backup generation has no reliability value at this constraint level. A fuel cell enters only in the off-grid case, and then only with 5 kW at Bizerte, where it supplies the night-time auxiliary load; the off-grid LCOH rises by 24–38% to 9.43–12.38 USD/kg because surplus electricity can no longer be exported and the reliability constraint becomes binding. Fuel cell backup would therefore become relevant only for stricter reliability targets, frequent multi-day outages or islanded operation, which are outside the present grid-connected base case.

3.8. Demand Profile and Electrolyzer Performance

Demand profile and level. The diurnal profile changes the LCOH by less than 0.3% and enlarges the tank by up to 11%, because the hydrogen buffer already decouples production from dispensing. The stochastic profile, with weekly and random daily variation, raises the LCOH by 1.3–2.1% and the tank by 20–48% (to 195–313 kg), while the electrolyzer changes by at most 3%; the reserve rule keeps the LPSP at zero although it uses the expected rather than the actual demand. Halving the demand to 50 kg/day raises the LCOH by 1.9–2.5%, and doubling it to 200 kg/day lowers it by 0.3–0.6%, reflecting the fixed auxiliary load and the minimum compressor size. Storage, rather than electrolyzer capacity, is therefore the design variable most sensitive to realistic refueling patterns.

Electrolyzer part load and degradation. With the load-dependent SEC of Equation (17a), the mean SEC falls to 54.4–54.5 kWh/kg, and the LCOH decreases by 0.5–0.7%, so the constant 55 kWh/kg is slightly conservative for the load profiles obtained here; the curve penalizes operation below 15% load, but the turndown limit keeps such hours rare. Degradation has a much larger effect. In case D1, frequent starts (360–570 per year) dominate the accumulated degradation; the stack life falls from 11–18 years to 3.9–4.7 years, the mean SEC rises to 57.5 kWh/kg, and the LCOH increases by 11–19%, with the largest increase at the PV-only Sousse site. The optimizer responds by adding wind capacity at the wind sites (for example from 716 to 849 kW at Bizerte), which smooths the electrolyzer input. In the stress case D2, the LCOH rizes by about 40–55%, and at three sites the optimizer installs 2.5–4.0 MWh of batteries with a minimum-size electrolyzer that runs almost continuously, reducing starts to about 20 per year. Degradation-aware operation can therefore change both the replacement schedule and the technology mix, which makes start-stop management a priority for field validation.

Compression temperature. Linking the suction temperature to the ambient temperature (Equation (18a)) makes w_c vary between 1.98 and 2.29 kWh/kg, with a mean of 2.10–2.11 kWh/kg, and changes the LCOH of the Table 4 designs by at most 0.011 USD/kg (0.1%). The constant 303 K assumption is therefore adequate for planning, although summer peaks raise the intercooler duty and the required compressor rating by up to 9%.

3.9. Probabilistic Uncertainty

A Monte Carlo analysis with 1000 samples propagated joint uncertainty in thirteen inputs through the Table 4 designs (Figure 9): PV, wind, electrolyzer, storage and compressor CAPEX (±23–30%), O&M rate (2–4%), discount rate (5–11%), project life (20–30 years), import and export tariffs (0.08–0.18 and 0–0.06 USD/kWh), stack life (50,000–100,000 h), a wind speed correction (1.0–1.2) and the daily demand (80–120 kg/day), all sampled uniformly and independently. The median LCOH is 7.58, 8.06, 8.25 and 9.67 USD/kg, with 5th to 95th percentile ranges of 5.46–10.08, 6.04–10.66, 6.16–10.97 and 7.06–13.11 USD/kg. Bizerte remains the cheapest site in 97.4% of the samples, Sousse the most expensive in 99.0%, and the complete ranking is preserved in 96.1%, because most uncertain inputs affect all sites in the same direction. The discount rate is the dominant input (Spearman coefficient 0.64–0.68), followed by the PV and electrolyzer CAPEX, the export tariff and the demand; wind CAPEX and wind speed matter only at the three wind sites. For fixed designs, the 90% renewable fraction is met in 51–70% of the samples, mainly because higher demand or weaker wind dilutes the renewable supply, while the LPSP limit is always met.

A reduced re-optimization of six joint samples per site confirmed the technology selection: the fuel cell was never selected, wind was always selected at Bizerte, Gabès and Ben Guerdane, and at Sousse wind entered only in the two samples that combined a wind speed correction above 15% with a wind CAPEX below about 1260 USD/kW.

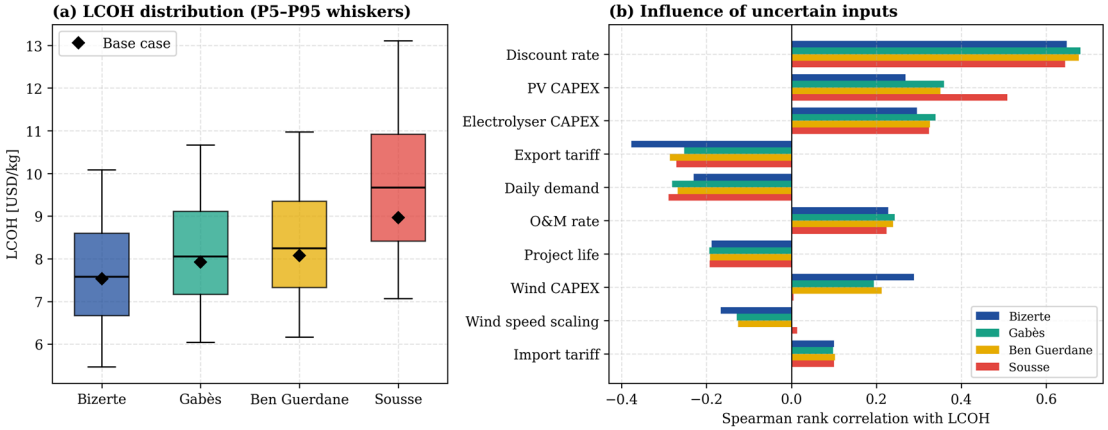

Figure 9. Monte Carlo uncertainty analysis.

4. Discussion

4.1. Cost Level and Comparison with Recent HRS Studies

The present LCOH range of 7.52–9.00 USD/kg is consistent with the order of magnitude reported for several recent refueling studies, although direct numerical comparison requires caution because currencies, station scale, electricity sourcing, storage pressure, and system boundaries differ. Mahmood et al. [11] reported 7.49 EUR/kg for a PV-powered railway HRS before crediting excess electricity sales, while Caponi et al. [12] obtained approximately 10.2–12 EUR/kg for grid-connected bus-fleet cases. Hajjaji and Cristofari [13] reported 6.95 EUR/kg for a larger 440 kg/day solar station, and Sgaramella et al. [31] obtained 9.22 EUR/kg for an optimized HCNG refueling configuration. These comparisons place the present results within a credible station-scale range without implying one-to-one equivalence. Table 8 normalizes these values to USD at 1.08 USD/EUR, the 2023–2024 average reference rate, and adds two boundary-adjusted values of the present study. Without export revenue, the present LCOH is 8.19–9.91 USD/kg, and the production-only cost, which excludes the compressor and storage equipment, is 6.96–8.55 USD/kg. On this

basis, the present stations lie between the 440 kg/day Corsican solar station and the bus-fleet stations, and above the mega-scale production plants, as expected from their scale and system boundary.

Table 8. Normalized comparison of LCOH with recent studies.

Study	Scale and Boundary	Reported LCOH	LCOH (USD/kg)
Mahmood et al. [11]	Railway HRS, on-site PV electrolysis	7.49 EUR/kg	8.09
Caponi et al. [12]	Bus fleet HRS, grid-connected	10.2–12.0 EUR/kg	11.0–13.0
Hajjaji and Cristofari [13]	440 kg/day solar HRS	6.95 EUR/kg	7.51
Sgaramella et al. [31]	HCNG refueling station	9.22 EUR/kg	9.96
Haffaf and Lakdja [28]	Mega-scale production and storage	2.99–3.71 USD/kg	2.99–3.71
This study, full station	100 kg/day, with export credit	7.52–9.00 USD/kg	7.52–9.00
This study, no export revenue	100 kg/day, re-optimized	–	8.19–9.91
This study, production only	Excludes compressor and storage	–	6.96–8.55

Scale and system boundary explain part of the spread in published costs. For example, Haffaf and Lakdja [28] reported substantially lower LCOH values of 2.99–3.71 USD/kg for mega-scale solar-wind hydrogen production in Algeria. That study addresses large-scale production and storage rather than a retail refueling station with station-level compression, reliability, and grid-interaction constraints. Conversely, O'Neill et al. [6] showed that imposing stable hydrogen delivery can increase cost relative to a purely cost-optimized intermittent system. Together, these studies support comparing LCOH only after accounting for scale, delivery obligation, and boundary conditions.

4.2. Solar-Wind Complementarity and Technology Selection

The central multi-site result is that the sunniest location is not the least-cost location. Bizerte has the lowest annual irradiation among the four sites but reaches the minimum LCOH of 7.52 USD/kg because its stronger wind resource complements PV generation outside peak solar hours. Sousse, whose annual irradiation (1875 kWh/m^2) is intermediate and below that of Gabès and Ben Guerdane, has the weakest wind resource; meeting the 90% renewable-fraction target therefore requires substantial PV oversizing and raises LCOH to 9.00 USD/kg. Gabès and Ben Guerdane occupy an intermediate position because both PV and wind contribute to the optimal mix. This behavior is consistent with meteorological studies showing that solar-wind complementarity can reduce renewable variability [34–36] and with the multi-site hydrogen results reported for Algeria [28].

The additional contribution here is economic rather than purely meteorological: wind capacity is allowed to disappear from the solution when its resource is insufficient. The zero-wind solution at Sousse and the large wind capacities retained at Bizerte, Gabès, and Ben Guerdane show that, once capital cost, dispatch, storage, grid exchange, and reliability are considered together, the resource regime decides whether wind enters the design at all. At Sousse the optimizer excludes wind, so complementarity cannot be exploited there, and the design reverts to PV with hydrogen storage, whereas at the three other sites it is exploited through the PV-wind mix. The same conditional interpretation applies to flexibility technologies. Fuel-cell backup is not intrinsically uneconomic, but it was excluded in every grid-connected case tested, including unrestricted dispatch, import tariffs of 0.5 USD/kWh and multi-day outages, and entered only marginally in off-grid operation (Section 3.7). Likewise, the battery result depends on the assumed cost and changes materially below 120–150 USD/kWh at Sousse and only at 80 USD/kWh or less at the wind sites, consistent with the context-dependent storage competition described in [4,33].

4.3. Practical Implications and Transferability

For early-stage HRS planning, the results suggest that screening candidate sites by annual GHI alone can mis-rank locations. A joint assessment of solar and wind timing should precede detailed optimization, particularly when a high renewable fraction is imposed. In the present cases, stronger wind availability reduces the need for extreme PV oversizing and provides renewable energy outside daylight hours. This finding is relevant to coastal North African planning, where both resources can vary substantially over relatively short geographic distances.

The numerical capacities and LCOH values should not be transferred directly to another country or station size. The more transferable result is the design logic: use long-horizon resource data, allow competing flexibility technologies to enter or leave the optimum, and evaluate renewable targets together with local grid tariffs and dispensing requirements. For Tunisia, this means that renewable hydrogen planning should combine resource complementarity, station demand, grid conditions, and technology prices rather than treating solar potential as the sole site-selection metric.

Transferability to other regions. The numerical results apply to coastal sites with similar resource regimes, cost levels, and grid access. Elsewhere, the transferable elements are the method and three conditional rules obtained here: wind entered the least-cost design at hub-height capacity factors of about 22% and above but not at 18% or below; battery storage became material below about 120–150 USD/kWh for a PV-dominated site and only at 80 USD/kWh or less where wind complements PV; and, with grid access, a hydrogen buffer of 1.5–3 days of demand, rather than a fuel cell, provided the multi-day flexibility. These thresholds depend on the cost assumptions of Table 3 and should be recomputed for other markets.

Most significant results for practice. From a design and operation perspective, the most significant results are that (i) sites should be screened by joint solar and wind behavior over many years rather than by annual irradiation, since this ordering survived all scenarios except one stress case and 96% of the Monte Carlo samples; (ii) the hydrogen tank and electrolyzer oversizing, not batteries or fuel cells, provide the flexibility of a grid-connected station, and storage is the variable most affected by refueling patterns; and (iii) start-stop degradation of the electrolyzer is the operating issue with the largest cost leverage, so control strategies that limit cycling deserve priority.

Representativeness of the EMS. The rule-based EMS represents a conservative hourly station controller with a 12 h demand reserve and no weather forecast. Real stations dispense in discrete fills, cycle compressors and cascade storage on sub-hourly time scales and may use predictive control [15,16]. The reliability metric therefore measures the energy adequacy of the hydrogen supply rather than service quality at the dispenser, such as queueing or pressure recovery between back-to-back fills. The import cap scenario also showed that the reserve rule recovers the tank more aggressively than necessary, so an optimized or predictive dispatch would likely lower the LCOH slightly rather than change the technology selection.

4.4. Limitations and Research Needs

The meteorological input is the principal data limitation. ERA5-Land provides a spatially consistent hourly record [46], but it is a reanalysis product rather than a site measurement. Moreover, Baas [48] recently reported systematic under-representation of ERA5-Land 10 m wind speeds relative to ERA5 in several regions. That finding has not been independently quantified for the Tunisian sites considered here. The absolute wind-energy estimates and wind-sensitive capacity decisions should therefore be validated with local mast or LiDAR measurements, or repeated with ERA5 wind fields, before investment-grade use. Applying the same product to all four sites supports internal comparison

but does not eliminate systematic bias. The bias test of Section 3.7 bounds this limitation for the ranking and for the selection of wind, but not for absolute energy yields.

The economic results are also scenario-dependent. The 100 kg H_2/day duty is representative rather than measured at each site, and the import/export tariffs of 0.12/0.04 USD/kWh are base-case assumptions. Larger throughput could lower unit cost by spreading balance-of-plant expenditure, while different tariff or feed-in structures could change the value of grid exchange and the preferred storage mix. The battery threshold and zero fuel-cell capacity should therefore be interpreted as conditional outcomes of the stated assumptions rather than universal technology rankings. Sections 3.7–3.9 quantify the most important of these dependencies.

Finally, the hourly model does not resolve sub-hourly electrical transients or detailed compressor dynamics. Degradation is represented through operating-hour stack lives in the base case and through the voltage degradation scenarios of Section 3.8, whose start penalties are assumptions rather than measured values. The Monte Carlo analysis treats the inputs as independent and propagates them mainly through fixed designs, so it does not represent correlated cost trajectories or a full stochastic optimization. These simplifications are appropriate for planning-level sizing but limit claims about real-time control and lifetime operation.

Strength of the conclusions. Because the plant models are simplified and the dispatch is rule-based, the conclusions differ in strength. Directly supported by the optimization and robust across the tested scenarios are the site ranking, the exclusion of wind at Sousse, the exclusion of the fuel cell with grid access, and the role of the hydrogen buffer. Conditional on the stated assumptions are the absolute LCOH values, the battery thresholds, the renewable premium, and the value of export revenue. Experimental or field validation is still required for the absolute wind yields, the electrolyzer degradation and start-stop behavior, and the dispenser-level reliability. Future work should therefore combine site measurements, dispensing records and degradation data from operating stations with a predictive or optimization-based dispatch.

5. Conclusions

This paper quantified how long-term solar-wind complementarity affects the techno-economic sizing of grid-connected renewable hydrogen refueling stations on the Tunisian coast. Four sites were evaluated over 2015–2025 using the same hourly plant model, reserve-aware dispatch logic, reliability requirement, renewable-fraction target, and sizing procedure. The analysis was designed to identify the preferred component mix under a common set of assumptions rather than to propose a new optimization algorithm.

The principal findings are:

1. LCOH ranges from 7.52 to 9.00 USD/kg under the 90% renewable-fraction target, with zero hydrogen supply loss in the base-case optima. Generation and electrolysis remain the dominant cost contributions. Ten independent PSO runs per site agree within 0.4%.
2. Solar-wind complementarity changes the site ranking. Bizerte achieves the lowest LCOH despite the lowest annual irradiation because wind generation complements PV output, whereas wind-poor Sousse requires substantial PV oversizing and has the highest cost. The ranking held in all scenarios except the D2 degradation stress case and in 96% of the Monte Carlo samples.
3. Under the assumed grid tariffs and component costs, fuel-cell capacity is not selected, and battery capacity remains small at 300 USD/kWh. Fuel cell capacity also remains zero with unrestricted dispatch, import tariffs of 0.5 USD/kWh, and multi-day outages. Battery storage becomes material below 120–150 USD/kWh at Sousse and only

at 80 USD/kWh or less at the wind sites, confirming that technology selection is scenario-dependent.

4. Increasing the renewable fraction from the unconstrained optimum to 90% raises the LCOH by 5.6–15.0% across the four sites, mainly through additional generation and electrolyzer capacity, while sharply reducing grid imports. Renewable targets therefore have a measurable and non-linear cost consequence.
5. Electrolyzer degradation driven by start-stop cycling is the largest operational cost risk identified: a moderate degradation scenario shortens the stack life to about 4 years and raises the LCOH by 11–19%, whereas part-load efficiency and compression temperature change it by less than 1%.

The main conclusion is therefore not that one technology is universally superior, but that, for the four coastal sites and the reanalysis data used here, multi-year joint solar-wind behavior materially affects HRS design when renewable-share and reliability constraints are enforced. This conclusion survived a 20% wind speed correction, but its absolute magnitude still requires validation with site measurements. The numerical results remain conditional on ERA5-Land, the representative 100 kg H_2/day duty, the stated tariffs, and planning-level component models. Independent wind-resource validation, site-specific demand data, and measured electrolyzer degradation are the next priorities for investment-grade assessment.

Author Contributions: Conceptualization, M.E.A., F.B.N., M.A.Z. and C.B.S.; Methodology, M.E.A., F.B.N. and C.B.S.; formal analysis, M.E.A., F.B.N., A.A. and C.B.S.; data curation, M.E.A., F.B.N., and C.B.S.; visualization, M.E.A., F.B.N., A.A. and C.B.S.; writing (original draft preparation), M.E.A., F.B.N. and C.B.S.; writing (review and editing), M.E.A., F.B.N., M.A.Z., A.A. and C.B.S.; investigation, M.E.A., F.B.N. and C.B.S.; software, M.E.A., F.B.N. and C.B.S.; validation, M.E.A., F.B.N., M.A.Z. and C.B.S.; project administration, M.A.Z., A.A. and C.B.S.; supervision, M.E.A., M.A.Z., A.A. and C.B.S.; resources, M.E.A., F.B.N., M.A.Z. and C.B.S. All authors have read and agreed to the published version of the manuscript.

Funding: The authors received no financial support for the research, authorship, or publication of this article.

Data Availability Statement: ERA5-Land input data are publicly available through the Copernicus Climate Data Store. Processed data and analysis code supporting the reported results are available from the corresponding author upon reasonable request.

Acknowledgments: The authors gratefully acknowledge Baseem Khan (Department of Electrical and Electronic Engineering Technology, University of Johannesburg, South Africa) for his constructive discussions, technical advice, and careful review of the manuscript, which significantly contributed to improving the quality of this work.

Conflicts of Interest: The authors declare no known competing financial interests or personal relationships that could have influenced the work reported in this paper.

Nomenclature

Symbol	Meaning	Unit
A_{mod}, A_{PV}	Module area; PV array area	m^2
a_0, a_1, a_2	Fuel cell part-load coefficients	–
C_{ann}	Annualized cost	USD/year
C_{cap}	Installed capital cost	USD
C_{op}	Annual operating cost	USD/year
$C_{\mathrm{rep},i}$	Present value of replacements of component i	USD
c	Weibull scale parameter	m/s

c_1, c_2	PSO cognitive and social coefficients	–
c_i^{cap}, c_i^{om}	Unit capital and O&M cost of component i	USD/unit; USD/(unit·year)
d	Real discount rate	–
E_b, E_b^{cap}	Battery energy content and capacity	kWh
e_{disp}	Specific auxiliary energy of dispensing	kWh/kg
F	Faraday constant	C/mol
$F(\mathbf{x})$	Penalized PSO fitness	USD/kg
$f(v)$	Weibull probability density	s/m
f_{RE}, $f_{\mathrm{RE}}^{\min}$	Renewable fraction and its minimum	–
$f_{\mathrm{H_2}}$	Renewable share of hydrogen	–
G, G_{STC}	Irradiance; irradiance at STC	W/m²
g_j	Normalized constraint function	–
$\mathbf{g}$	Global best position	–
H	Reserve look-ahead horizon	h
h_{op}	Stack operating hours since replacement	h
$\mathrm{HHV}_{\mathrm{H_2}}$, $\mathrm{LHV}_{\mathrm{H_2}}$	Higher and lower heating value of hydrogen	kWh/kg
I_{el}	Stack current	A
k	Weibull shape parameter; PSO iteration index	–
$k_{\max}$	Maximum number of PSO iterations	–
L_b, L_b^{cal}, L_i	Battery life; calendar life; component life	years
$M_{\mathrm{H_2}}$, $M_{\mathrm{H_2O}}$	Molar masses of hydrogen and water	kg/mol
$M_{\mathrm{H_2}}^{\mathrm{yr}}$	Annual hydrogen delivered	kg/year
$\dot{m}_{\mathrm{H_2}}^{\mathrm{dem}}$, $\dot{m}_{\mathrm{H_2}}^{\mathrm{disp}}$	Hydrogen demand and dispensing rates	kg/h
$\dot{m}_{\mathrm{H_2}}^{\mathrm{el}}$, $\dot{m}_{\mathrm{H_2}}^{\mathrm{fc}}$	Hydrogen production and fuel cell consumption rates	kg/h
$\dot{m}_{\mathrm{H_2O}}$	Feedwater demand	kg/h
m_{st}, $m_{\mathrm{st}}^{\min}$, $m_{\mathrm{st}}^{\max}$	Stored hydrogen mass and its bounds	kg
m_{res}	Hydrogen reserve	kg
N	Project life	years
N_c, N_{PV}	Number of cells; number of PV modules	–
N_{cyc}	Rated battery cycle life	cycles
N_{ss}	Number of electrolyzer starts	–
n_s	Number of compression stages	–
P_{PV}, P_{WT}, P_{WT}^{ρ}	PV power; wind power; density-corrected wind power	kW
P_{STC}, P_r	Module rating at STC; turbine rated power	kW
P_b^{ch}, P_b^{dis}, $P_b^{\max}$	Battery charge, discharge and maximum power	kW
P_{el}, $P_{\mathrm{el}}^{\min}$, $P_{\mathrm{el}}^{\mathrm{rated}}$	Electrolyzer power; minimum and rated power	kW
P_c, P_c^r	Compressor power and rating	kW
P_{fc}, $P_{\mathrm{fc}}^{\min}$, P_{fc}^r	Fuel cell power; minimum and rated power	kW
$P_{\mathrm{grid}}^{\mathrm{imp}}$, $P_{\mathrm{grid}}^{\mathrm{exp}}$, $P_{\mathrm{grid}}^{\max}$	Grid import, export and PCC limit	kW
P_{load}, P_{aux}	Station auxiliary load; base auxiliary load	kW
P_{net}, ΔP	Net renewable power; surplus or deficit	kW
p_{in}, p_{out}, p_{st}	Suction, discharge and tank pressure	bar
p_{sp}	Surface pressure	Pa
$\mathbf{p}_i$	Personal best position of particle i	–
R, R_a	Universal gas constant; specific gas constant of air	J/(mol·K); J/(kg·K)
r_1, r_2	Uniform random numbers	–
r_V	Cell voltage degradation rate	μV/h
S_i	Rating of component i	kW, kWh or kg
SEC, SEC_r	Specific energy consumption; rated value	kWh/kg
SOC, $\mathrm{SOC}_{\min}$, $\mathrm{SOC}_{\max}$, $\mathrm{SOC}_{\mathrm{res}}$	State of charge, limits and reserve	–
T_{amb}, T_{cell}, T_{STC}	Ambient, cell and STC temperature	°C

T_{in}, T_{st}	Suction and tank temperature	K
t, Δt	Time index; time step	h
V_0, V_r	Cell voltage at zero and rated current density	V
V_{st}	Tank volume	m^3
v_{10}, v_h	Wind speed at 10 m and at hub height	m/s
v_{ci}, v_r, v_{co}	Cut-in, rated and cut-out speed	m/s
$\mathbf{v}_i$	Velocity of particle i	–
w, $w_{\max}$, $w_{\min}$	PSO inertia weight and its limits	–
w_c	Specific compression work	kWh/kg
$\mathbf{x}$, $\mathbf{x}_i$	Design vector; position of particle i	–
Z	Compressibility factor	–
z_h, z_{10}	Hub height; reference height	m
α	Wind shear exponent	–
β_{bop}	Electrolyzer balance-of-plant share	–
γ	Heat capacity ratio of hydrogen	–
γ_P	PV power temperature coefficient	1/K
ΔT_{ic}	Intercooler approach temperature	K
δ	Relative voltage degradation	–
$\varepsilon_{\mathrm{H_2}}$	LPSP limit	–
η_{ch}, η_{dis}	Battery charge and discharge efficiency	–
η_{conv}, η_{dr}	Converter efficiency; PV derating factor	–
η_{el}, η_F	Electrolyzer efficiency; Faraday efficiency	–
η_{fc}, η_{fc}^0	Fuel cell efficiency; rated value	–
η_{is}	Overall compressor efficiency	–
κ_{ss}	Equivalent operating hours per start	h
λ	Electrolyzer load ratio	–
λ_w	Feedwater surplus ratio	–
μ_j	Penalty weight	USD/kg
π_{imp}, π_{exp}	Import and export tariffs	USD/kWh
$\pi_{\mathrm{fc}}^{\mathrm{th}}$	Fuel cell dispatch price threshold	USD/kWh
ρ_a, ρ_0	Air density; reference air density	kg/m^3
τ	Look-ahead time index	h
φ_i	Replaced cost share of component i	–
χ_{exp}	Export cap fraction	–
CAPEX	Capital expenditure	–
CRF	Capital recovery factor	–
DoD	Depth of discharge	–
EMS	Energy management strategy	–
GHI	Global horizontal irradiation	–
HRS	Hydrogen refueling station	–
LCOH	Levelized cost of hydrogen	–
LFP	Lithium iron phosphate	–
LPSP	Loss-of-supply probability	–
NOCT	Nominal operating cell temperature	–
NPC	Net present cost	–
O&M	Operation and maintenance	–
PCC	Point of common coupling	–
PEM	Proton exchange membrane	–
PSO	Particle swarm optimization	–
PV	Photovoltaic	–
SEC	Specific energy consumption	–
STC	Standard test conditions	–
SWRO	Seawater reverse osmosis	–

https://doi.org/10.3390/en19225633

References

1. Zun, M.T.; McLellan, B.C. Cost projection of global green hydrogen production scenarios. *Hydrogen* **2023**, *4*, 932–960. https://doi.org/10.3390/hydrogen4040055.
2. Liu, H.; Clausen, L.R.; Wang, L.; Chen, M. Pathway toward cost-effective green hydrogen production by solid oxide electrolyzer. *Energy Environ. Sci.* **2023**, *16*, 2090–2111. https://doi.org/10.1039/D3EE00232B.
3. Reksten, A.H.; Thomassen, M.S.; Møller-Holst, S.; Sundseth, K. Projecting the future cost of PEM and alkaline water electrolysers; a CAPEX model including electrolyser plant size and technology development. *Int. J. Hydrogen Energy* **2022**, *47*, 38106–38113. https://doi.org/10.1016/j.ijhydene.2022.08.306.
4. Abdelsalam, R.A.; Mohamed, M.; Farag, H.E.Z.; El-Saadany, E.F. Green hydrogen production plants: A techno-economic review. *Energy Convers. Manag.* **2024**, *319*, 118907. https://doi.org/10.1016/j.enconman.2024.118907.
5. Guilbert, D.; Papakonstantinou, G. Modeling, degradation study, failures diagnosis and faulty operating management of electrolyzers. *Membranes* **2022**, *12*, 1195. https://doi.org/10.3390/membranes12121195.
6. O'Neill, K.T.; Jiao, F.; Al Ghafri, S.; May, E.F.; Johns, M.L. Stable electrolytic hydrogen production using renewable energy. *Energy Convers. Manag.* **2024**, *321*, 119070. https://doi.org/10.1016/j.enconman.2024.119070.
7. Gado, M.G.; Nasser, M.; Hassan, H. Potential of solar and wind-based green hydrogen production frameworks in African countries. *Int. J. Hydrogen Energy* **2024**, *68*, 520–536. https://doi.org/10.1016/j.ijhydene.2024.04.272.
8. Farhani, S.; Barhoumi, E.M.; Grissa, H.; Ouda, M.; Bacha, F. A techno-economic feasibility study of electricity and hydrogen production in hybrid solar-wind energy park: The case study of Tunisian Sahel. *Eng. Technol. Appl. Sci. Res.* **2024**, *14*, 15154–15160. https://doi.org/10.48084/etasr.7394.
9. Bdioui, H.; Touati, H.; Ben Chiekh, M.; López-Agüera, A. Green hydrogen blending into the Tunisian natural gas distributing system. *Hydrogen* **2024**, *5*, 54. https://doi.org/10.3390/hydrogen5040054.
10. Zúñiga-Saiz, P.; Sánchez-Díaz, C. Design of a hydrogen refueling station with hydrogen production by electrolysis, storage and dispensing for a bus fleet in the city of Valencia. *Int. J. Hydrogen Energy* **2025**, *104*, 651–664. https://doi.org/10.1016/j.ijhydene.2024.07.387.
11. Mahmood, M.A.; Pérez de la Calle, P.; Meneses Zuluaga, J.M.; Massarotti, N.; Sánchez-Díaz, C. Techno-economic evaluation of hydrogen refuelling station with on-site electrolysis production powered by photovoltaic solar energy for the railway sector. *Int. J. Hydrogen Energy* **2025**, *138*, 802–822. https://doi.org/10.1016/j.ijhydene.2025.05.094.
12. Caponi, R.; Bocci, E.; Del Zotto, L. On-site hydrogen refuelling station techno-economic model for a fleet of fuel cell buses. *Int. J. Hydrogen Energy* **2024**, *71*, 691–700. https://doi.org/10.1016/j.ijhydene.2024.05.216.
13. Hajjaji, M.; Cristofari, C. Economic and technical evaluation of on-site electrolysis solar hydrogen refueling station in Corsica: A case study of Ajaccio. *Renew. Energy* **2024**, *231*, 120982. https://doi.org/10.1016/j.renene.2024.120982.
14. Abbas, Q.; Ali, H.M.; Alquaity, A.B.S. Techno-economic analysis of renewable energy systems with pumped hydro storage for desalinating water in Saudi Arabia. *Int. J. Thermofluids* **2025**, *30*, 101430. https://doi.org/10.1016/j.ijft.2025.101430.
15. Cardona, P.; Costa-Castelló, R.; Roda, V.; Carroquino, J.; Valiño, L.; Ocampo-Martinez, C.; Serra, M. Modelling and operation strategy approaches for on-site hydrogen refuelling stations. *Int. J. Hydrogen Energy* **2024**, *52*, 49–64. https://doi.org/10.1016/j.ijhydene.2023.08.192.
16. Cardona, P.; Costa-Castelló, R.; Roda, V.; Carroquino, J.; Valiño, L.; Serra, M. Model predictive control of an on-site green hydrogen production and refuelling station. *Int. J. Hydrogen Energy* **2023**, *48*, 17995–18010. https://doi.org/10.1016/j.ijhydene.2023.01.191.
17. Kim, G.-W.; Park, S.-W.; Son, S.-Y. Techno-economic optimal operation of an on-site hydrogen refueling station. *Appl. Sci.* **2025**, *15*, 10999. https://doi.org/10.3390/app152010999.
18. Wu, S.; Lin, J.; Li, J.; Song, Y. Electricity allocation strategy for on-site hydrogen refueling stations in the forward and spot markets. *IET Renew. Power Gener.* **2022**, *16*, 2532–2546. https://doi.org/10.1049/rpg2.12406.
19. Amara, S.; Toumi, S.; Ben Salah, C.; Saidi, A.S. Improvement of techno-economic optimal sizing of a hybrid off-grid micro-grid system. *Energy* **2021**, *233*, 121166. https://doi.org/10.1016/j.energy.2021.121166.
20. Khiareddine, A.; Ben Salah, C.; Rekioua, D.; Mimouni, M.F. Sizing methodology for hybrid photovoltaic/wind/hydrogen/battery integrated to energy management strategy for pumping system. *Energy* **2018**, *153*, 743–762. https://doi.org/10.1016/j.energy.2018.04.073.
21. Asaduz-Zaman, M.; Ramli, M.A.M.; Alghamdi, S. Techno-economic optimization of autonomous PV/wind/battery microgrid for seawater reverse osmosis desalination plant. *IEEE Access* **2025**, *13*, 199417–199453. https://doi.org/10.1109/ACCESS.2025.3635344.

22. Mbouteu Megaptche, C.A.; Kim, H.; Musau, P.M.; Waita, S.; Aduda, B. Techno-economic comparative analysis of two hybrid renewable energy systems for powering a simulated house, including a hydrogen vehicle load at Jeju Island. *Energies* **2023**, *16*, 7836. https://doi.org/10.3390/en16237836.
23. AL-bonsrulah, H.A.Z.; Alshukri, M.J.; Mikhaeel, L.M.; AL-sawaf, N.N.; Kefif, N.; Reddy, M.V.; Zaghib, K. Design and simulation studies of hybrid power systems based on photovoltaic, wind, electrolyzer, and PEM fuel cells. *Energies* **2021**, *14*, 2643. https://doi.org/10.3390/en14092643.
24. Park, J.; Kang, S.; Kim, S.; Cho, H.-S.; Heo, S.; Lee, J.H. Techno-economic analysis of solar powered green hydrogen system based on multi-objective optimization of economics and productivity. *Energy Convers. Manag.* **2024**, *299*, 117823. https://doi.org/10.1016/j.enconman.2023.117823.
25. Li, R.; Jin, X.; Yang, P.; Zheng, M.; Zheng, Y.; Cai, C.; Sun, X.; Luo, Z.; Zhao, L.; Huang, Z.; et al. Capacity optimization of a wind-photovoltaic-electrolysis-battery (WPEB) hybrid energy system for power and hydrogen generation. *Int. J. Hydrogen Energy* **2024**, *52*, 311–333. https://doi.org/10.1016/j.ijhydene.2023.08.029.
26. Al-Mahmodi, M.; Ayadi, O.; Wang, Y.; Al-Halhouli, A. Sensitivity-based techno-economic assessment approach for electrolyzer integration with hybrid photovoltaic-wind plants for green hydrogen production. *Int. J. Hydrogen Energy* **2025**, *97*, 904–919. https://doi.org/10.1016/j.ijhydene.2024.12.002.
27. Oueslati, F.; Fezai, S. Optimal techno-economic design of PV-wind hydrogen refueling stations (HRFS) for 20 selected Saudi sites. *Wind Eng.* **2024**, *48*, 1055–1075. https://doi.org/10.1177/0309524X241247229.
28. Haffaf, A.; Lakdja, F. Mega-scale solar-wind complementarity assessment for large-scale hydrogen production and storage (H2PS) in Algeria: A techno-economic analysis. *Int. J. Hydrogen Energy* **2024**, *86*, 985–1009. https://doi.org/10.1016/j.ijhydene.2024.08.443.
29. Belboul, Z.; Toual, B.; Bensalem, A.; Ghenai, C.; Khan, B.; Kamel, S. Techno-economic optimization for isolated hybrid PV/wind/battery/diesel generator microgrid using improved salp swarm algorithm. *Sci. Rep.* **2024**, *14*, 2920. https://doi.org/10.1038/s41598-024-52232-y.
30. Mohamed, M.A.; Eltamaly, A.M. *Modeling and Simulation of Smart Grid Integrated with Hybrid Renewable Energy Systems*; Studies in Systems, Decision and Control, Volume 121; Springer: Cham, Switzerland, 2018. https://doi.org/10.1007/978-3-319-64795-1.
31. Sgaramella, A.; Pastore, L.M.; Lo Basso, G.; Mojtahed, A.; de Santoli, L. HCNG refuelling station to accelerate the transition towards a real hydrogen economy: A techno-economic analysis. *Int. J. Hydrogen Energy* **2024**, *69*, 1403–1416. https://doi.org/10.1016/j.ijhydene.2024.05.145.
32. Abdollahipour, A.; Sayyaadi, H. Optimal design of a hybrid power generation system based on integrating PEM fuel cell and PEM electrolyzer as a moderator for micro-renewable energy systems. *Energy* **2022**, *260*, 124944. https://doi.org/10.1016/j.energy.2022.124944.
33. Beuse, M.; Steffen, B.; Schmidt, T.S. Projecting the competition between energy-storage technologies in the electricity sector. *Joule* **2020**, *4*, 2162–2184. https://doi.org/10.1016/j.joule.2020.07.017.
34. Hajou, A.; El Mghouchi, Y.; Chaoui, M. A new solar-wind complementarity index: An application to the climate of Morocco. *Renew. Energy* **2024**, *227*, 120490. https://doi.org/10.1016/j.renene.2024.120490.
35. Muchiri, K.; Kamau, J.N.; Wekesa, D.W.; Saoke, C.O.; Mutuku, J.N.; Gathua, J.K. Wind and solar resource complementarity and its viability in wind/PV hybrid energy systems in Machakos, Kenya. *Sci. Afr.* **2023**, *20*, e01599. https://doi.org/10.1016/j.sciaf.2023.e01599.
36. Sabovcik, R.; Mykhalchyk Hradicky, J.; Sinka, M. Leveraging open-source data to study solar-wind complementarity in the global perspective. *Renew. Energy Focus* **2024**, *50*, 100583. https://doi.org/10.1016/j.ref.2024.100583.
37. Roslan, M.-F.; Ramachandaramurthy, V.K.; Mansor, M.; Mokhzani, A.S.; Jern, K.P.; Begum, R.A.; Hannan, M.A. Techno-economic impact analysis for renewable energy-based hydrogen storage integrated grid electric vehicle charging stations in different potential locations of Malaysia. *Energy Strategy Rev.* **2024**, *54*, 101478. https://doi.org/10.1016/j.esr.2024.101478.
38. Buttler, A.; Spliethoff, H. Current status of water electrolysis for energy storage, grid balancing and sector coupling via power-to-gas and power-to-liquids: A review. *Renew. Sustain. Energy Rev.* **2018**, *82*, 2440–2454. https://doi.org/10.1016/j.rser.2017.09.003.
39. Feng, Q.; Yuan, X.-Z.; Liu, G.; Wei, B.; Zhang, Z.; Li, H.; Wang, H. A review of proton exchange membrane water electrolysis on degradation mechanisms and mitigation strategies. *J. Power Sources* **2017**, *366*, 33–55. https://doi.org/10.1016/j.jpowsour.2017.09.006.
40. Republic of Tunisia. *Law No. 2015-12 of 11 May 2015 on the Production of Electricity from Renewable Energies*; Official Journal of the Republic of Tunisia: Tunis, Tunisia, 2015.

41. Reddi, K.; Elgowainy, A.; Rustagi, N.; Gupta, E. Impact of hydrogen refueling configurations and market parameters on the refueling cost of hydrogen. *Int. J. Hydrogen Energy* **2017**, *42*, 21855–21865. https://doi.org/10.1016/j.ijhydene.2017.05.122.
42. European Commission. Commission Delegated Regulation (EU) 2023/1184 of 10 February 2023 supplementing Directive (EU) 2018/2001 by establishing a Union methodology setting out detailed rules for the production of renewable liquid and gaseous transport fuels of non-biological origin. *Off. J. Eur. Union* **2023**, *L 157*, 11–19.
43. Muñoz-Sabater, J.; Dutra, E.; Agustí-Panareda, A.; Albergel, C.; Arduini, G.; Balsamo, G.; Boussetta, S.; Choulga, M.; Harrigan, S.; Hersbach, H.; et al. ERA5-Land: A state-of-the-art global reanalysis dataset for land applications. Earth Syst. Sci. Data 2021, 13, 4349–4383. https://doi.org/10.5194/essd-13-4349-2021.
44. Shi, Y.; Eberhart, R. A modified particle swarm optimizer. In Proceedings of the 1998 IEEE International Conference on Evolutionary Computation, Anchorage, AK, USA, 4–9 May 1998; pp. 69–73. https://doi.org/10.1109/ICEC.1998.699146.
45. Eberhart, R.C.; Shi, Y. Comparing inertia weights and constriction factors in particle swarm optimization. In Proceedings of the 2000 Congress on Evolutionary Computation, La Jolla, CA, USA, 16–19 July 2000; pp. 84–88. https://doi.org/10.1109/CEC.2000.870279.
46. Clerc, M.; Kennedy, J. The particle swarm - explosion, stability, and convergence in a multidimensional complex space. *IEEE Trans. Evol. Comput.* **2002**, *6*, 58–73. https://doi.org/10.1109/4235.985692.
47. Hersbach, H.; Bell, B.; Berrisford, P.; Hirahara, S.; Horányi, A.; Muñoz-Sabater, J.; Nicolas, J.; Peubey, C.; Radu, R.; Schepers, D.; et al. The ERA5 global reanalysis. *Q. J. R. Meteorol. Soc.* **2020**, *146*, 1999–2049. https://doi.org/10.1002/qj.3803.
48. Baas, A.C.W. Systematic under-representation of ERA5 10 m wind speeds in the ERA5-Land product undermines wind energy studies. *Appl. Energy* **2026**, *412*, 127634. https://doi.org/10.1016/j.apenergy.2026.127634.
49. Gandoin, R.; Garza, J. Underestimation of strong wind speeds offshore in ERA5: Evidence, discussion and correction. *Wind Energy Sci.* **2024**, *9*, 1727. https://doi.org/10.5194/wes-9-1727-2024.
50. Ramon, J.; Lledó, L.; Torralba, V.; Soret, A.; Doblas-Reyes, F.J. What global reanalysis best represents near-surface winds? *Q. J. R. Meteorol. Soc.* **2019**, *145*, 3236–3251. https://doi.org/10.1002/qj.3616.

Disclaimer/Publisher's Note: The statements, opinions and data contained in all publications are solely those of the individual author(s) and contributor(s) and not of MDPI and/or the editor(s). MDPI and/or the editor(s) disclaim responsibility for any injury to people or property resulting from any ideas, methods, instructions or products referred to in the content.